
# A deterministic talk(?) about stochastic calculations in classical and quantum physics

**Magnus Ögren**

*School of Science and Technology*

*Örebro University, Sweden*

2024-03-15

# Abstract:

In this personal overview talk I will introduce some applications of stochastic differential equations I have used, introduced, and improved, in my research in the last 15 years. It started in Brisbane, Australia, where I implemented (suggested by my supervisor) the first calculation for many-particle quantum dynamics with the so called Gaussian Phase-Space Representation (GPSR) [1,2].

Then I had a (2.nd) postdoc in Copenhagen, Denmark, actually during my first postdoc there I met Fatkhulla Abdullaev in Copenhagen in 2011! But during this second postdoc I was confronted with diffusion problems in classical physics where the computational domain where large and complicated 3D porous media from STM images of rock-samples (funded by the oil industry…). I then realized that I could apply some of the methods I had used in the quantum problem, while some techniques on boundary conditions needed to be developed [3,4]. During more recent years, after coming back more to research after heavy teaching duties, I have returned to those kinds of problems in Örebro, Sweden, where both Fatkhulla and Jasur Yuldashev have been. The new research has especially been along the following three avenues: 1) The classical Stefan problem for heat conduction with a moving ice-/water-interface [5,6]; 2) Implementing fermionic-Truncated-Wigner-Approximation (fTWA), with postdoc Francois Rousse [7], interrupted by covid [8]; 3) Attacking the fundamental problem with GPSR, to extend its applicability to more problems in quantum dynamics, by introducing so called matrix-equation-based diffusion gauges [9].

## Articles classical :

Ögren, M. (2014). Local boundary conditions for NMR-relaxation in digitized porous media. *The European Physical Journal B*, 87 (11), 255. (arXiv:1312.6581)

Ögren, M., Jha, D., Dobberschütz, S., Müter, D., Carlsson, M., Gulliksson, M., Stipp, S. & Sørensen, H. (2019). Numerical simulations of NMR relaxation in chalk using local Robin boundary conditions. *Journal of magnetic resonance*, 308. (arXiv:1909.09618)

*Book chapter:* Ögren, M., *Stochastic Solutions of Stefan Problems with General Time-Dependent Boundary Conditions.* In: Malyarenko, A., Ni, Y., Rancic, M., Silvestrov, S. (eds) Stochastic Processes, Statistical Methods, and Engineering Mathematics . SPAS 2019. Springer Proceedings in Mathematics & Statistics, vol 408. Springer, Cham. (https://doi.org/10.1007/978-3-031-17820-7_29), (arXiv:2006.04939 [math.AP]).

The role of super-spreaders in modeling of SARS-CoV-2, F Rousse, M Carlsson, M Ogren, B K.-Wellander
**Infectious Disease Modelling 7 (2022) 778-794**
https://arxiv.org/abs/2212.04545

**Random walks and moving boundaries: Estimating the penetration of diffusants into dense rubbers**
**Authors:** Surendra Nepal, Magnus Ogren, Yosief Wondmagegne, Adrian Muntean
**Probabilistic Engineering Mechanics 74 (2023) 103546,**
**arXiv:2305.08520 [pdf, other]** math.NA math.PR

*In progress:* Edström D., Ögren, M., Budaev B. (2024?). Stochastic solutions of multi-phase Stefan problems.
*In the future?:* Applications with directly calculated gradients, electric currents, liquid flows.

## Articles Quantum problems:

[1] First-principles quantum dynamics for fermions: Application to molecular dissociation,
M. Ogren, K. V. Kheruntsyan, J. F. Corney
Europhys. Lett., 92 (2010) 36003
https://arxiv.org/abs/0910.4440

[2] Stochastic simulations of fermionic dynamics with phase-space representations,
M. Ogren, K. V. Kheruntsyan, J. F. Corney
Comp. Phys. Comm. 182, 1999 (2011)
https://arxiv.org/abs/1008.0970

[7] Correlated quantum dynamics of graphene,
F. Rousse, O. Eriksson, M. Ogren
Phys. Rev. B 107, 134306 (2023)
https://arxiv.org/abs/2212.04352

[9] Simulations of quantum dynamics with fermionic phase-space representations using numerical matrix factorizations as stochastic gauges,
F Rousse, M Fasi, A Dmytryshyn, M Gulliksson, M Ogren
J. Phys. A: Math. Theor. 57 (2024) 015303
https://arxiv.org/abs/2304.05149

# Why did I start with this *Quantum* research… Background:

Computer Physics Communications 182 (2011) 1999–2003

Contents lists available at ScienceDirect

Computer Physics Communications

www.elsevier.com/locate/cpc

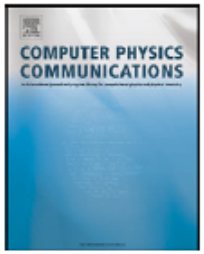


## Stochastic simulations of fermionic dynamics with phase-space representations

M. Ögren *, K.V. Kheruntsyan, J.F. Corney

*ARC Centre of Excellence for Quantum-Atom Optics, School of Mathematics and Physics, University of Queensland, Brisbane, Queensland 4072, Australia*

simulation. For Hamiltonians containing up to four operators, a second-order partial differential equation is generated, which can be written in the form of a Fokker–Planck equation (FPE):

$$\frac{d}{dt}P(\vec{\lambda}) = \left[-\sum_j \frac{\partial}{\partial\lambda_j}A_j(\vec{\lambda}) + \frac{1}{2}\sum_{j,k}\frac{\partial^2}{\partial\lambda_j\partial\lambda_k}D_{ij}(\vec{\lambda})\right]P(\vec{\lambda}). \qquad (5)$$

a mapping [14,15] to an equivalent set of stochastic differential equations (SDEs) to sample the moments of the distribution. In the Itō calculus, stochastic equations corresponding to Eq. (6) have the general form

$$\begin{aligned}
dn_{\mathbf{k}} &= \left(\alpha m_{\mathbf{k}}^{+} + \alpha^{+} m_{\mathbf{k}}\right)d\tau + N_0^{-1/2}\mathbf{B}^{(n_{\mathbf{k}})}\,\mathbf{dW},\\
dm_{\mathbf{k}} &= \left[-2i\delta_{\mathbf{k}}m_{\mathbf{k}} + \alpha(1-2n_{\mathbf{k}})\right]d\tau + N_0^{-1/2}\mathbf{B}^{(m_{\mathbf{k}})}\,\mathbf{dW},\\
dm_{\mathbf{k}}^{+} &= \left[2i\delta_{\mathbf{k}}m_{\mathbf{k}}^{+} + \alpha^{+}(1-2n_{\mathbf{k}})\right]d\tau + N_0^{-1/2}\mathbf{B}^{(m_{\mathbf{k}}^{+})}\,\mathbf{dW},\\
d\alpha &= -\frac{1}{N_0}\sum_{\mathbf{k}} m_{\mathbf{k}}\,d\tau + N_0^{-1/2}\mathbf{B}^{(\alpha)}\,\mathbf{dW},\\
d\alpha^{+} &= -\frac{1}{N_0}\sum_{\mathbf{k}} m_{\mathbf{k}}^{+}\,d\tau + N_0^{-1/2}\mathbf{B}^{(\alpha^{+})}\,\mathbf{dW}, \qquad (7)
\end{aligned}$$

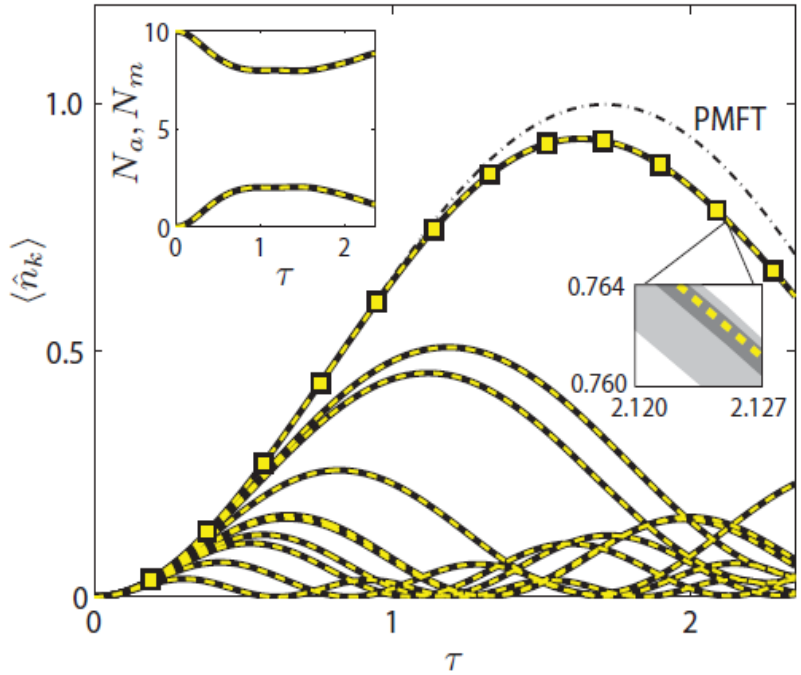


Fig. 1: (Color online) Comparison between different methods for the population dynamics of individual atomic modes $\langle \hat{n}_k(\tau) \rangle$: phase-space method with $10^6$ stochastic trajecto-

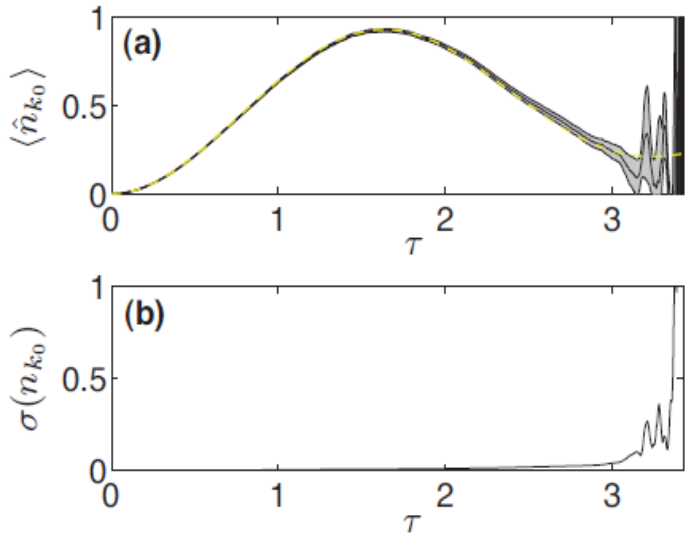


Fig. 2: (Color online) (a) Population of the resonant mode, $\langle \hat{n}_{k_0} \rangle$, as a function of time $\tau$ for the same parameters as in fig. 1, except with $10^3$ stochastic trajectories and a longer simulation time. The solid line is from the phase-space method, with the grey shading representing statistical errors of $\pm 1\sigma$

# Why did I start with this *Classical* research…
# Given a task (from funder!):

**Understand properties of large rocks from small samples…**

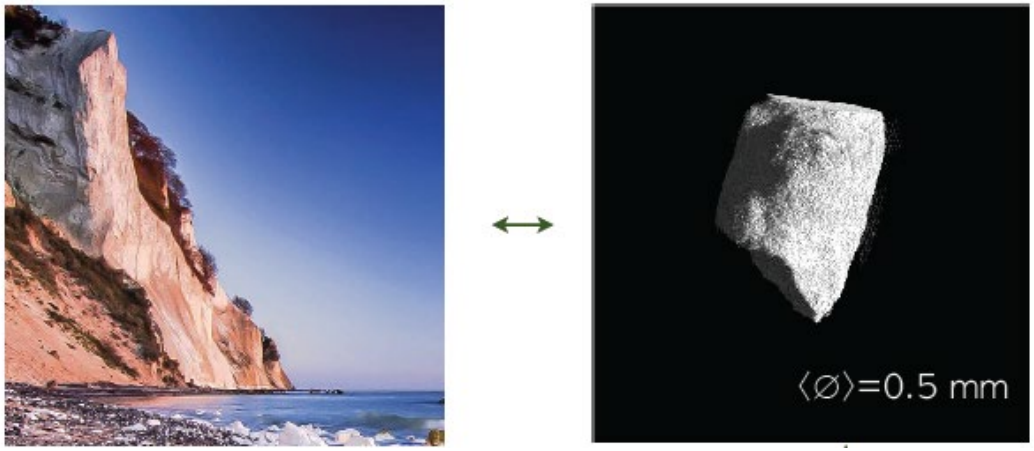


**Data from synchrotron radiation facilities.**

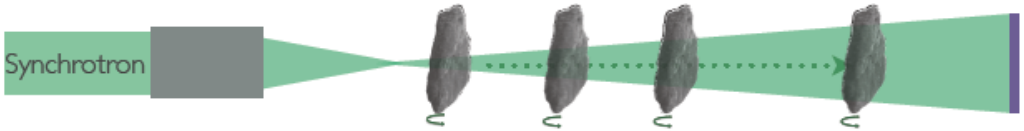


Measurement done at different positions in the conical beamline gives different resolution.

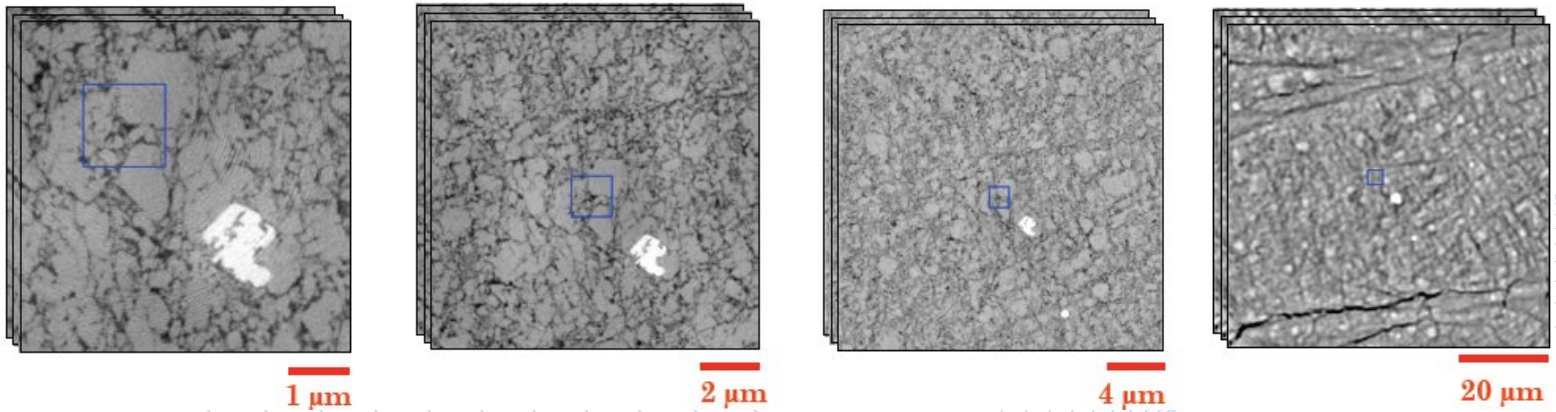

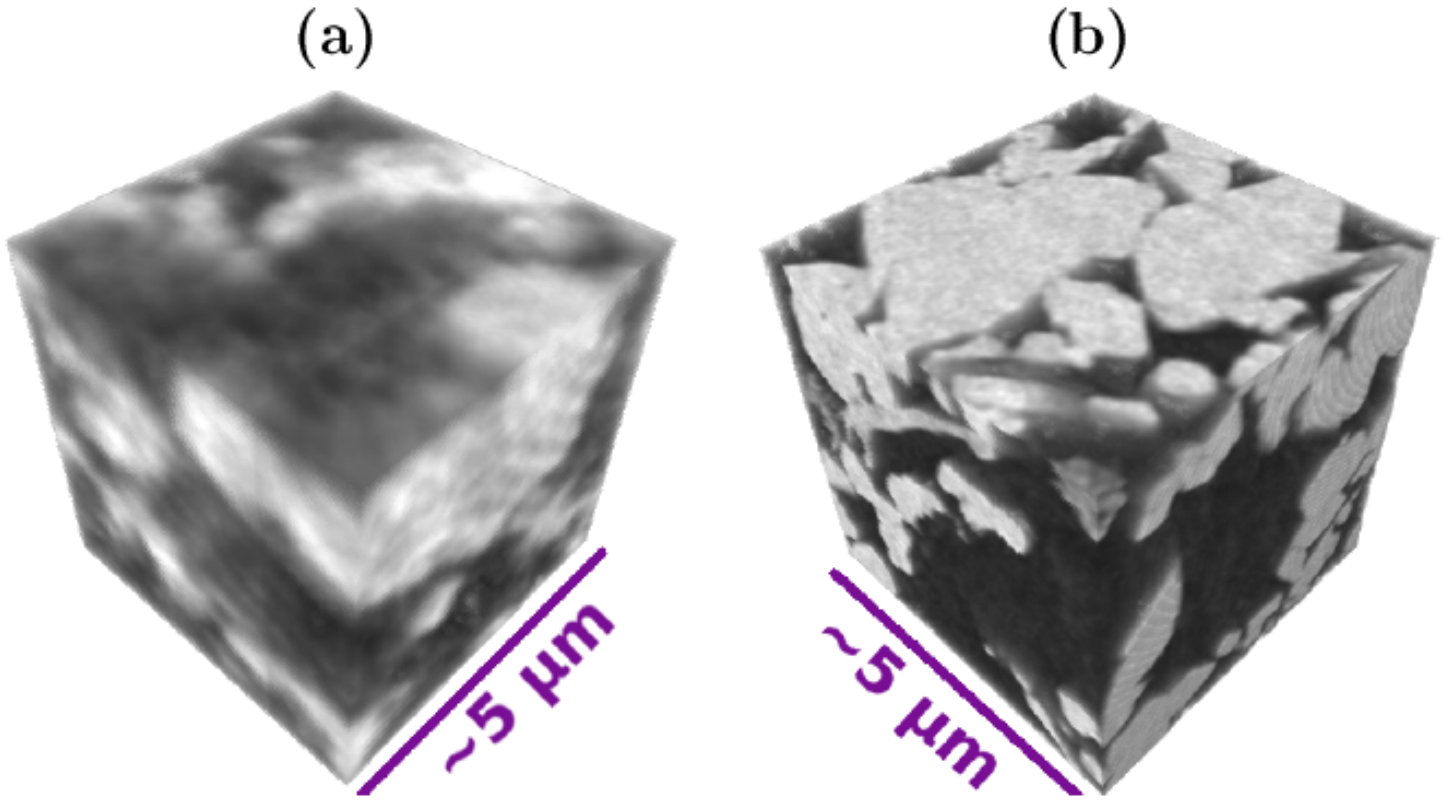


Figure 5: Examples of zooming in on regions in the CT-images for the two 3D chalk samples. To the left limestone (a) and to the right Aalborg chalk (b). Black ($Z = 1$) voxels constitutes the pore domain (assumed to be filled with brine). White ($Z = 0$) voxels represents regions of homogenous chalk. Aalborg chalk (b) contains a more complex pore morphology and was imaged with ptychographic X-ray nanotomography, which explains the sharper image compared to (a). Since the side length of the full samples are in the order of $N\Delta r \simeq 25$ µm (Table 2), the subvolumes shown here represents only about 1% of the chalk sample domains in our calculations.

# Moving boundaries….

A moving boundary problem for capturing the penetration of diffusant concentration into rubbers

Modeling, simulation and analysis

Surendra Nepal

from Nepal

CHAPTER 2. MODELING AND SIMULATION RESULTS

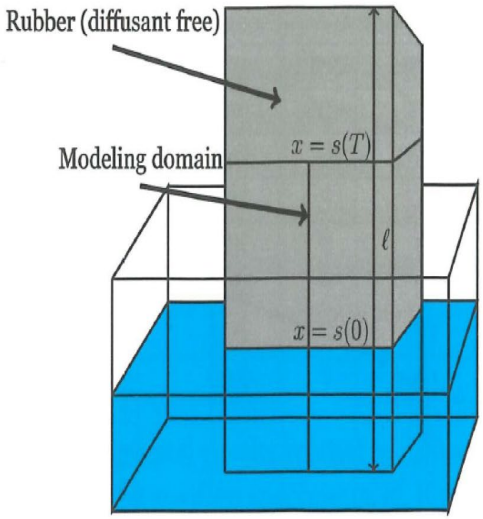


Figure 2.3.1: Sketch of the experimental setup. A rubber material is put in contact with a reservoir of diffusants.

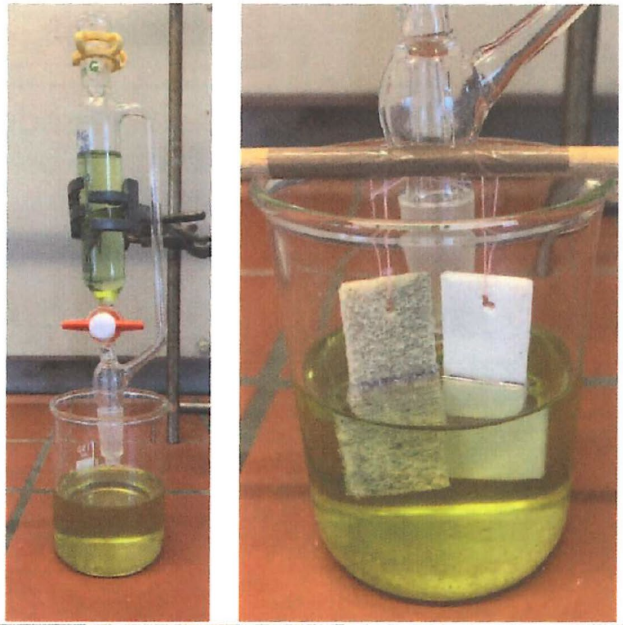

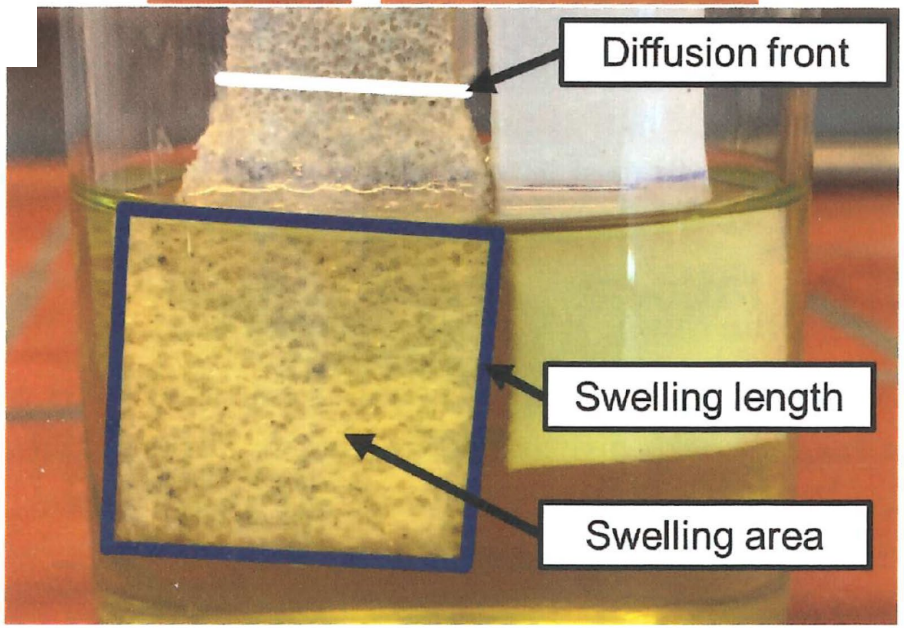


Figure 2.2.1: Experimental setup and evaluation.

# Nuclear Magnetic Resonance

## NMR important tool in modern technology.

## Mobile Ex Situ High Resolution NMR

**APPLICATIONS:**

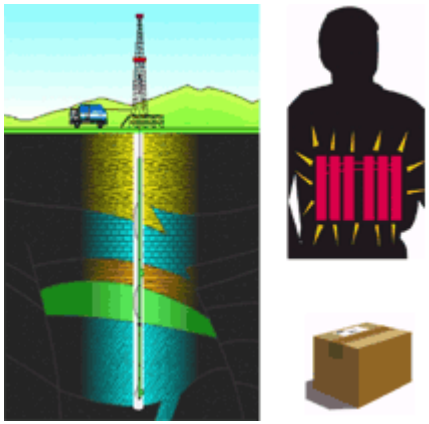

- Industrial sensing
- Oil well logging
- Medical imaging for large subjects
- Spectroscopy
- Imaging subjects or objects with ferromagnetic components
- Cargo inspection
- Stand-off detection

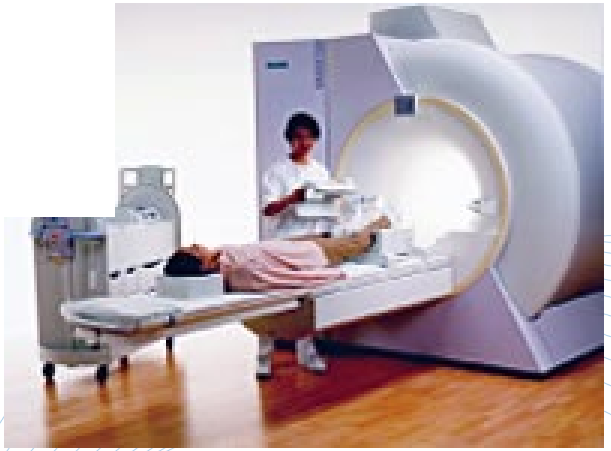

After simplifications of Bloch's equations

for NMR dynamics, we are left with a

reaction-diffusion equation

$$\frac{\partial M}{\partial t} = D_0 \nabla^2 M - \frac{M}{T_V},$$

with Robin boundary conditions

$$D_0 \mathbf{n} \cdot \nabla M + \rho M = 0.$$

We integrate out the spatial degrees

$$\mathcal{M}(t) = \int_{\Omega} M(\mathbf{x}, t)\, d\mathbf{x}$$

to obtain a time-dependent *total magnetization*

For uniform initial conditions, Gauss' theorem can provide the short time asymptote

$$\frac{1}{\mathcal{M}(0)} \left. \frac{d\mathcal{M}(t)}{dt} \right|_{t=0} = -\frac{\rho_0 S}{V}$$

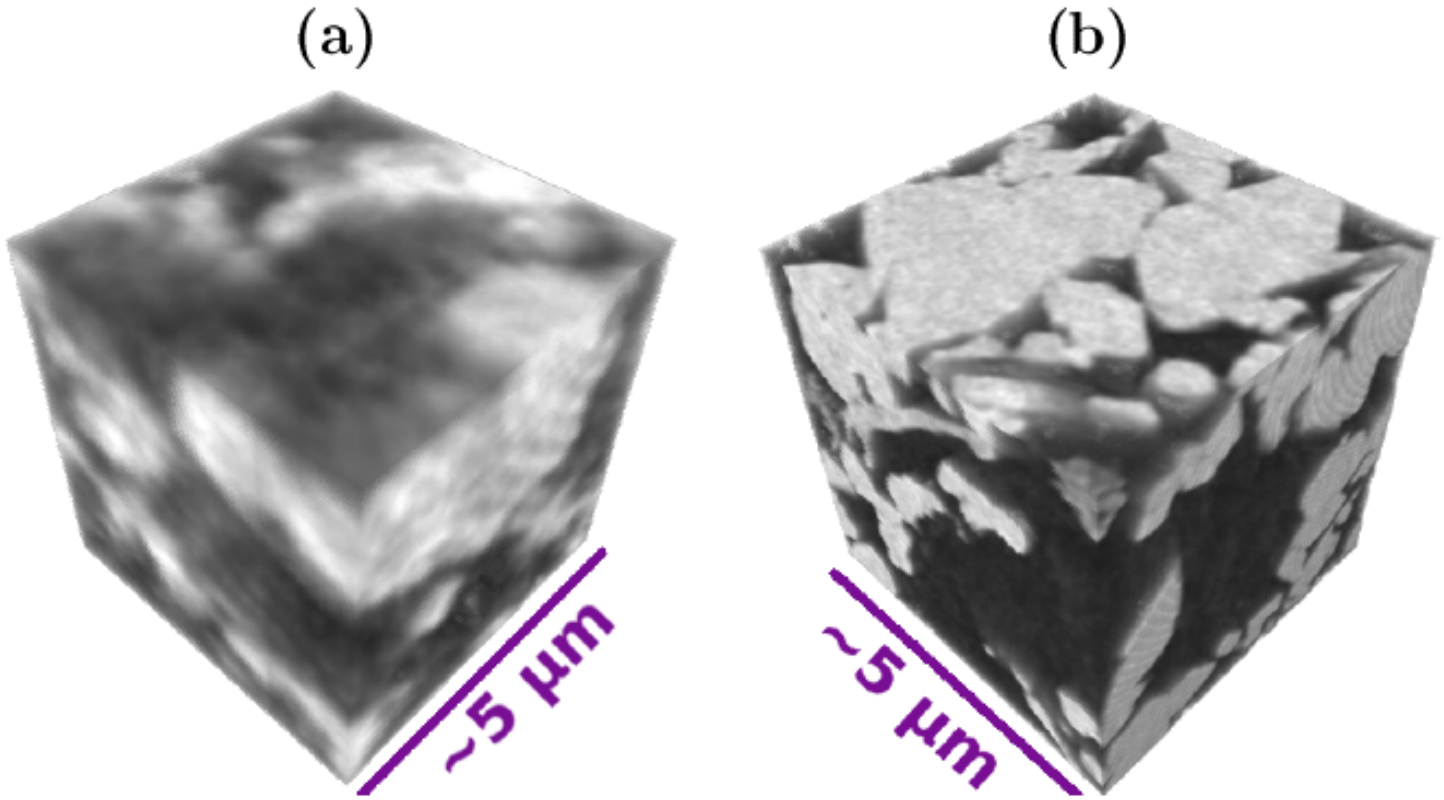


Figure 5: Examples of zooming in on regions in the CT-images for the two 3D chalk samples. To the left limestone (a) and to the right Aalborg chalk (b). Black ($Z = 1$) voxels constitutes the pore domain (assumed to be filled with brine). White ($Z = 0$) voxels represents regions of homogenous chalk. Aalborg chalk (b) contains a more complex pore morphology and was imaged with ptychographic X-ray nanotomography, which explains the sharper image compared to (a). Since the side length of the full samples are in the order of $N\Delta r \simeq 25$ µm (Table 2), the subvolumes shown here represents only about 1% of the chalk sample domains in our calculations.

# In many applications the domain can be problematic…

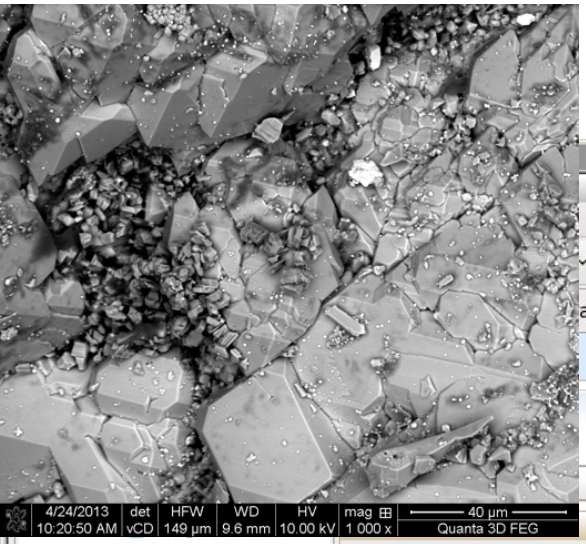

# Try a random approach!

*1.3.3. Random walk method* (*RWM*). The RWM can be applied to find the local solution of *second-order* partial differential equations of the form

$$\frac{\partial u(\mathbf{x},t)}{\partial t} = \sum_{i=1}^{d} \alpha_i(\mathbf{x}) \frac{\partial u(\mathbf{x},t)}{\partial x_i} + \frac{1}{2} \sum_{i,j=1}^{d} \beta_{ij}(\mathbf{x}) \frac{\partial^2 u(\mathbf{x},t)}{\partial x_i \, \partial x_j} + q(\mathbf{x},t)\, u(\mathbf{x},t) + p(\mathbf{x},t) \qquad (6)$$

where $\alpha_i, \beta_{ij}$ are real-valued functions defined on $\Re^d$, $d \geqslant 1$ is an integer, and $q, p$ denote real–valued functions defined on $\Re^d \times [0,\infty)$. The domain of definition of Equation (6) is $D \times (0,\infty)$, where $D \subset \Re^d$ is an open bounded set. The solution $u : D \times (0,\infty) \to \Re$ depends on the initial and boundary conditions that need to be specified. The operator of Equation (6) includes a large number of interesting special cases; for example, parabolic, hyperbolic, elliptic partial differential equations in $\Re^2$ correspond to the steady–state version of Equation (6) with $d = 2$ and $\beta_{12}(\mathbf{x})\,\beta_{12}(\mathbf{x}) - \beta_{11}(\mathbf{x})\,\beta_{22}(\mathbf{x}) = 0; > 0; < 0$, respectively. Therefore, for example, the Laplace, Poisson and Helmholtz equations are special cases of Equation (6).

The RWM method can be applied to find the local solution of Equation (6) with Dirichlet and/or Neumann boundary conditions. The solution by this method involves three steps. *First*, a diffusion process $\mathbf{X}$ with generator coinciding with the differential operator of Equation (6) has to be constructed. *Second*, a relationship needs to be established between the value of the unknown function $u$ at $(\mathbf{x},t) \in D \times (0,\infty)$, the boundary conditions, and an expectation depending on the sample paths of $\mathbf{X}$. Properties of diffusion processes, features of stochastic integrals, and Itô's formula can be used to obtain this relationship. *Third*, a Monte Carlo algorithm needs to be developed to estimate the expectation giving $u(\mathbf{x},t)$.

When discussing the convergence of a stochastic calculation we need to mention:

1) A large enough number of trajectories to obtain a statistically significant result;

2) A small enough step-size to explore the small scale geometry of the media. The latter issue is also directly connected to the resolution chosen for a digital media.

If conditions 1) and 2) are fulfilled, one can accuratelly simulate diffusion processes with Dirichlet ($\rho_0 \to \infty$) and Neumann ($\rho_0 \to 0$) boundary conditions in Eq. (4). However, for Robin boundary conditions we need to consider also a third point.

3) Probability based modeling of the surface relaxation, including:

3a) a correct (algorithm dependent) relation between the local probability for surface relaxation ($p_a$) and the function $\rho_0(\mathbf{x}, t)$;

3b) A local description of the surface area for a digital media.

**3a)** We have derived (first order) relation between parameters in PDE model and the RWM:

$$p_S = \Delta r \rho / D_0.$$

**3b)** We have constructed (first order) local boundary conditions that can be calculated "on the fly":

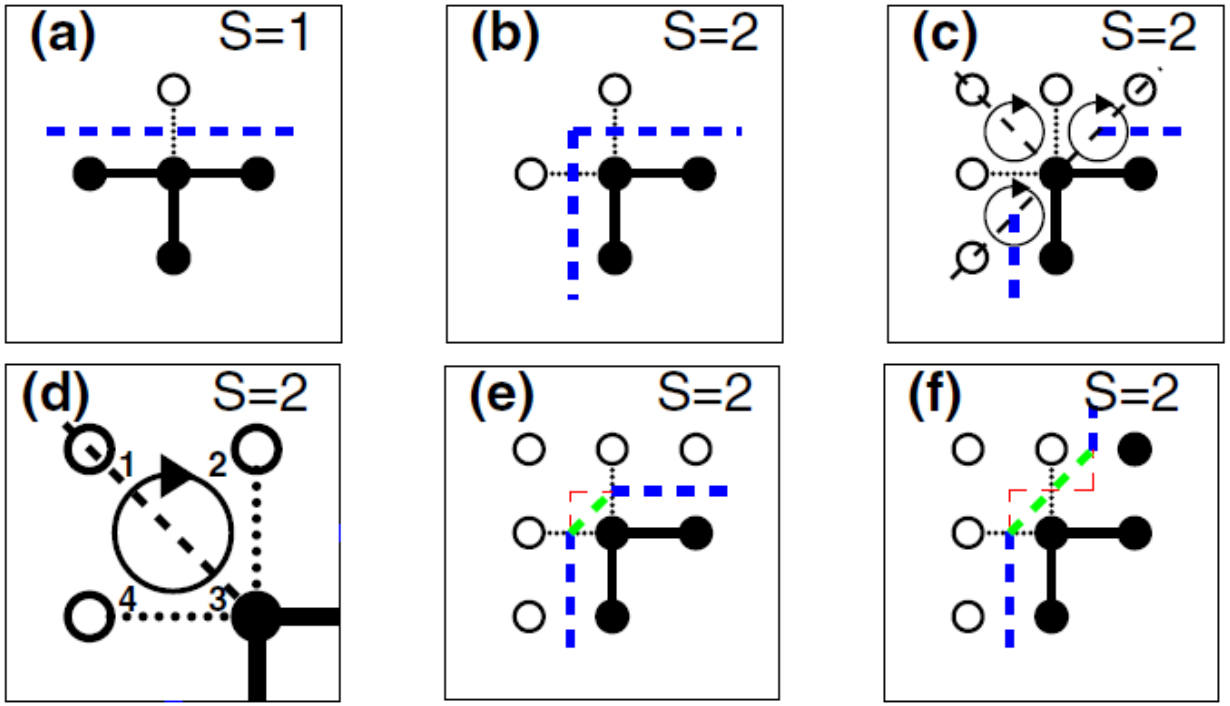


Above illustrated in 2D, generalized to any dimension.

# In 2D the effects of ‘digitalization’ is easy to illustrate and quantify:

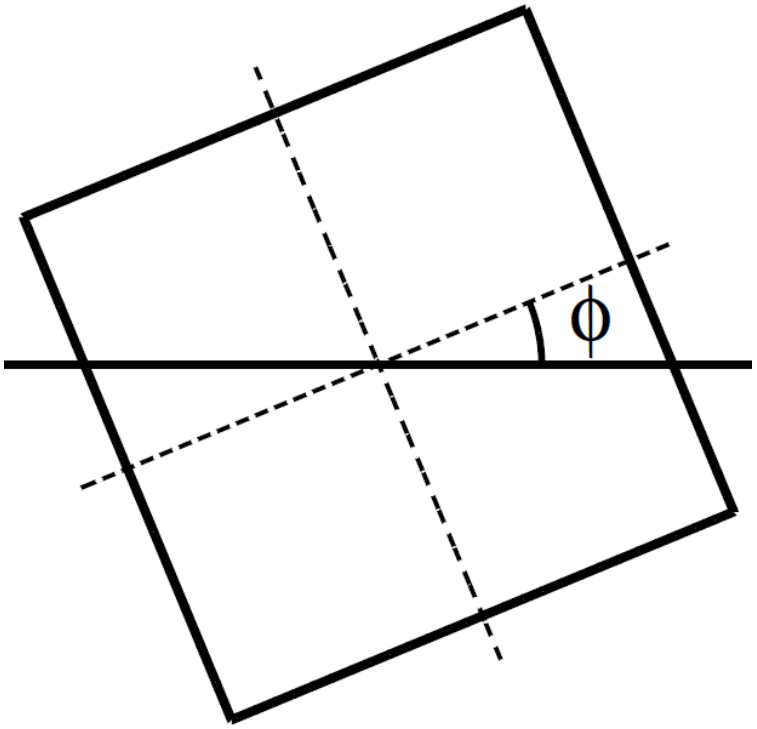


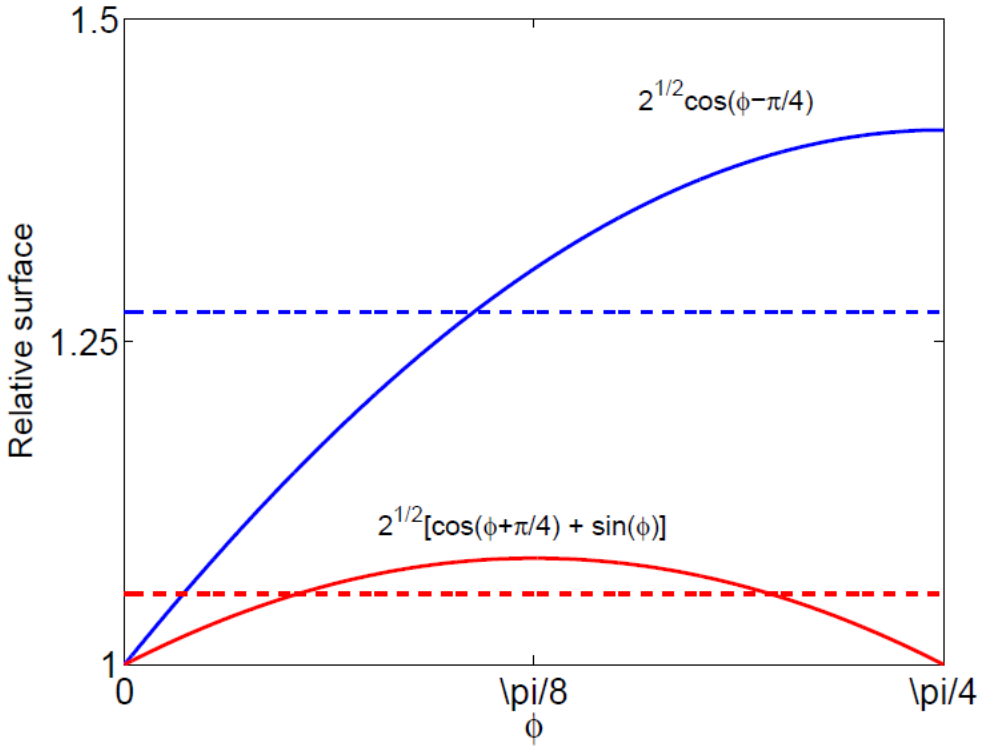

# Comparative FEM simulations in 2D.

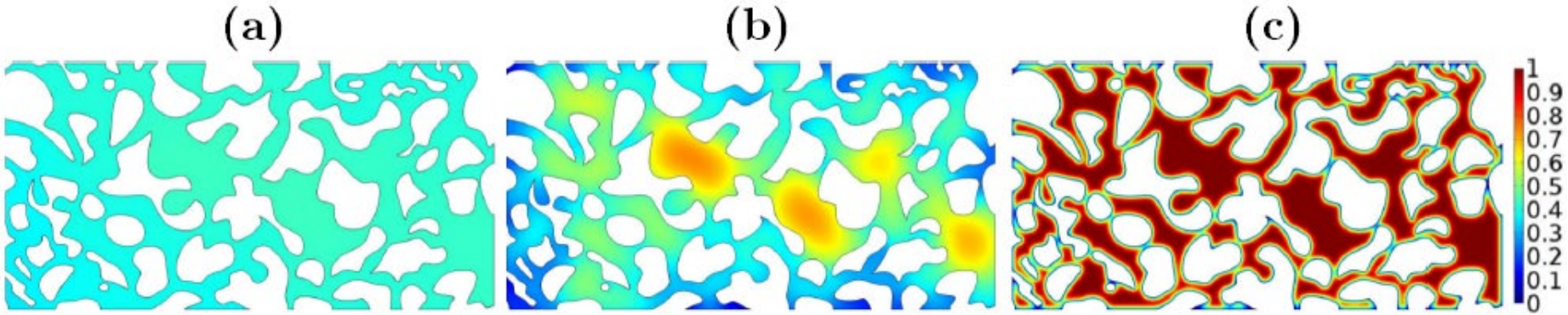


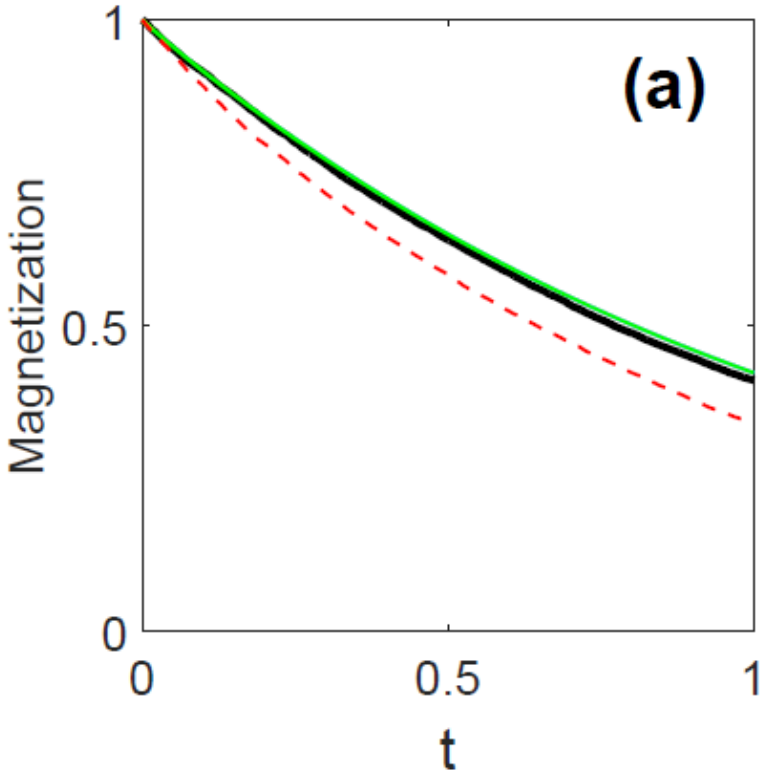

# Comparison with analytic formulae: *Ball*

$$\mathcal{M}(t) = \mathcal{M}(0)\, 12 \sum_{j=1}^{\infty} \frac{\left[\sin\left(\sqrt{\lambda_j}\right) - \sqrt{\lambda_j}\cos\left(\sqrt{\lambda_j}\right)\right]^2}{\lambda_j^{3/2}\left[2\sqrt{\lambda_j} - \sin\left(2\sqrt{\lambda_j}\right)\right]} \exp\left(-\frac{D_0}{R_0^2}\lambda_j t\right), \quad (8)$$

where the eigenvalues $\lambda_j$ are solutions of the equation $1 - \sqrt{\lambda_j}\cot\left(\sqrt{\lambda_j}\right) = R_0\rho/D_0$.

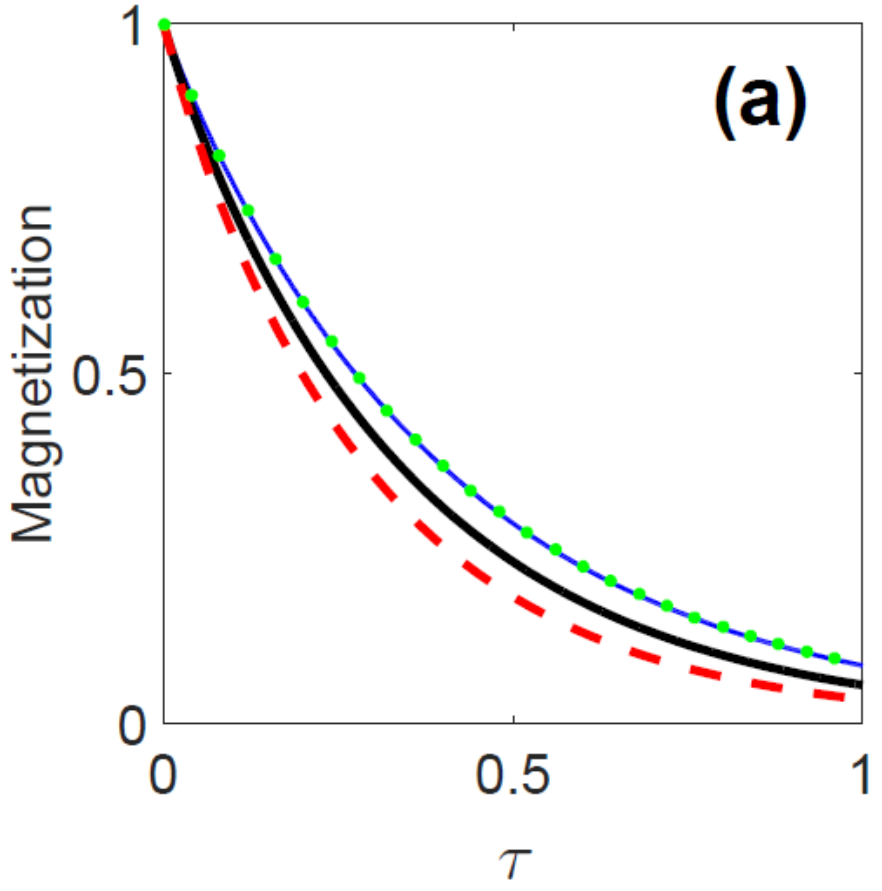


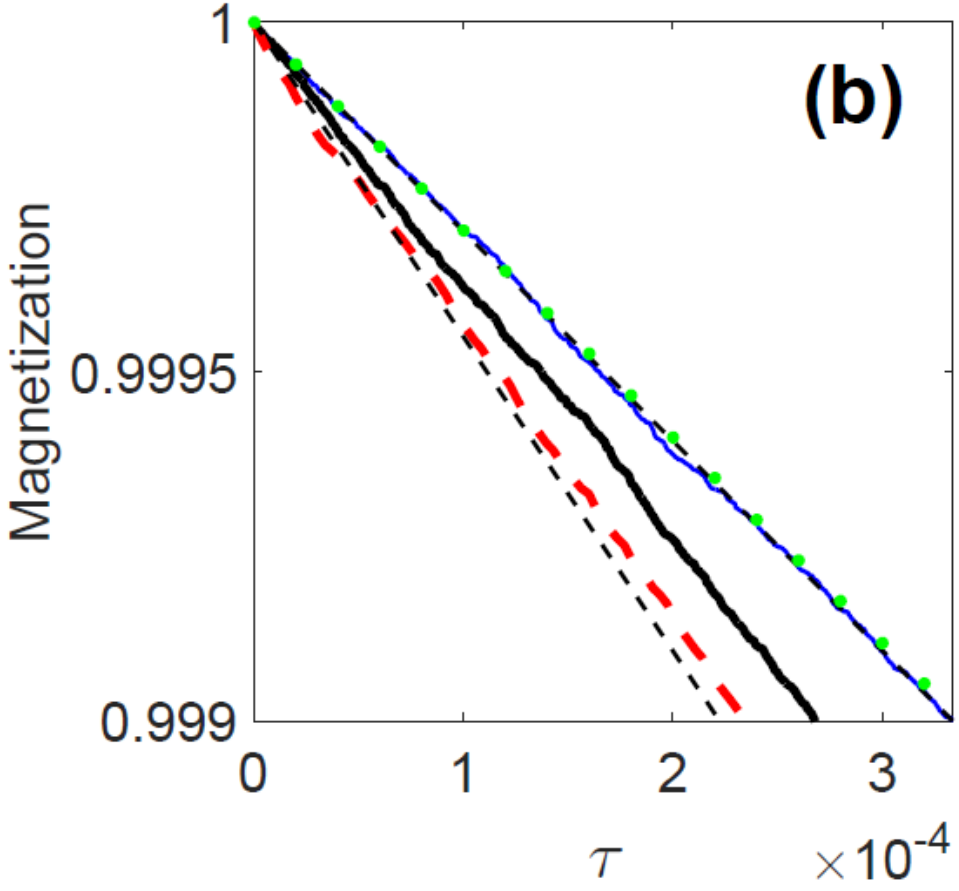

# Comparison with analytic formulae: *Cube*

$$\mathcal{M}(t) = \mathcal{M}(0)\, 8 \left[ \sum_{j=1}^{\infty} \frac{\sin^2\left(\sqrt{\lambda_j}\right)}{\sqrt{\lambda_j}\sin\left(\sqrt{\lambda_j}\right)\cos\left(\sqrt{\lambda_j}\right) + \lambda_j} \exp\left( -\frac{D_0}{R_0^2} \lambda_j t \right) \right]^3, \quad (9)$$

where the eigenvalues $\lambda_j$ are solutions of the equation $\sqrt{\lambda_j}\tan\left(\sqrt{\lambda_j}\right) = R_0\rho/D_0$.

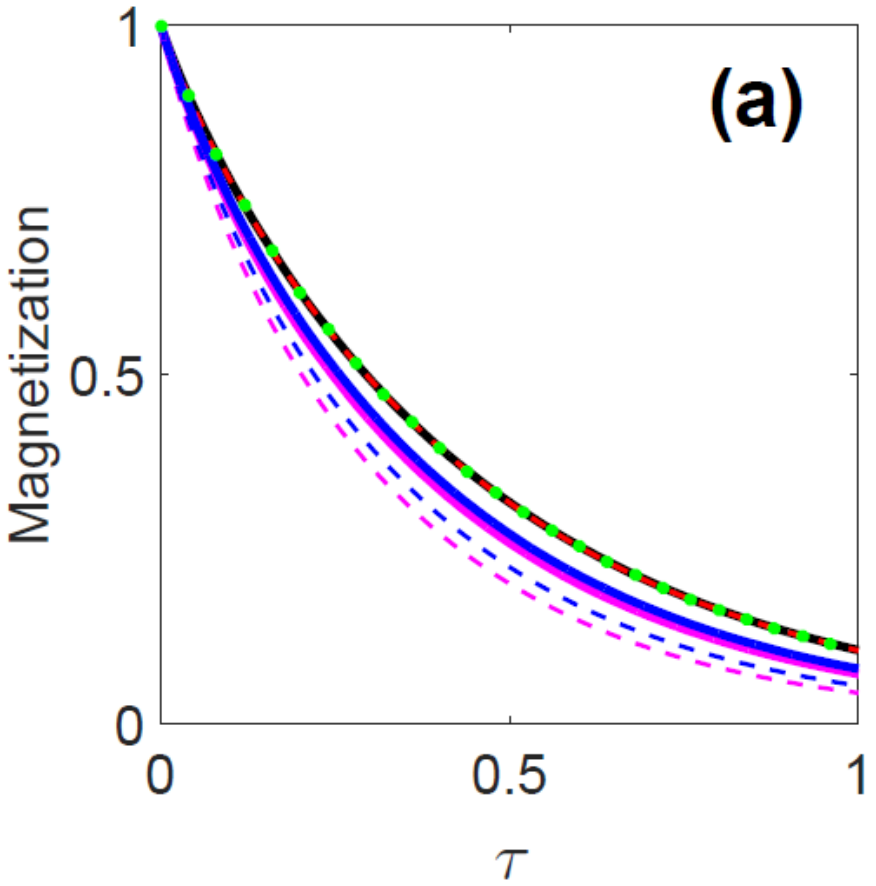


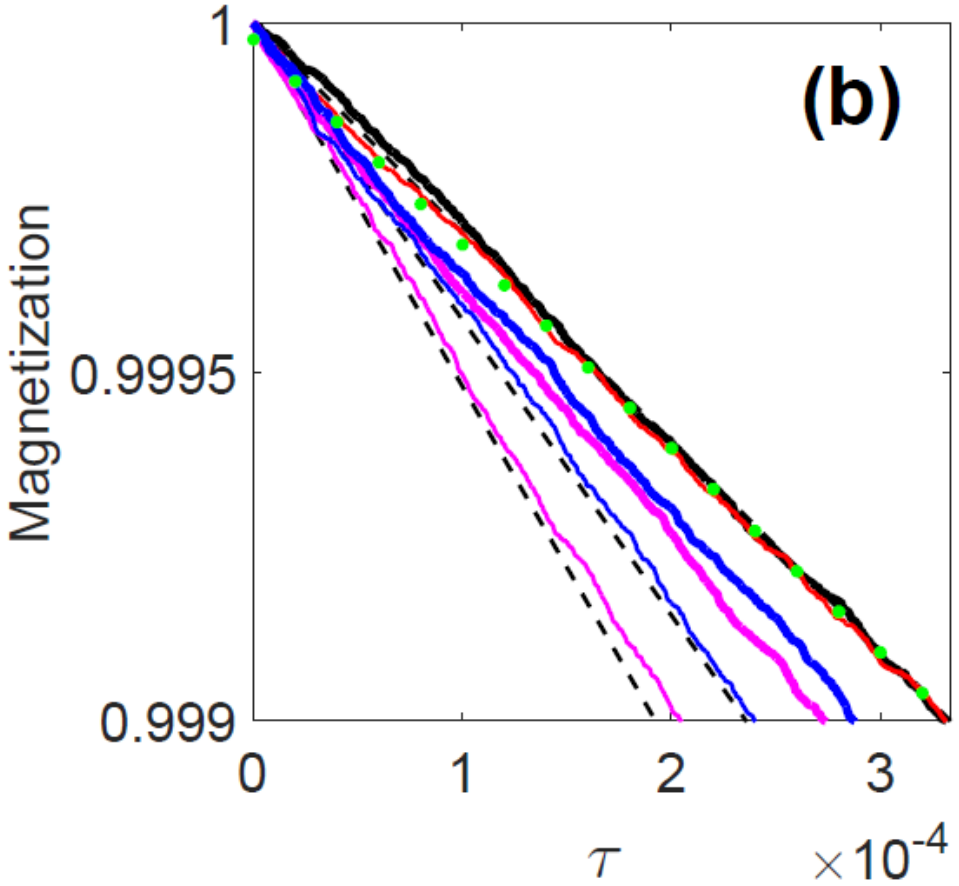

# Simulations on 3D tomography images of chalk with a size in the order of $10^3 \times 10^3 \times 10^3$ voxels and resolution 10 nm

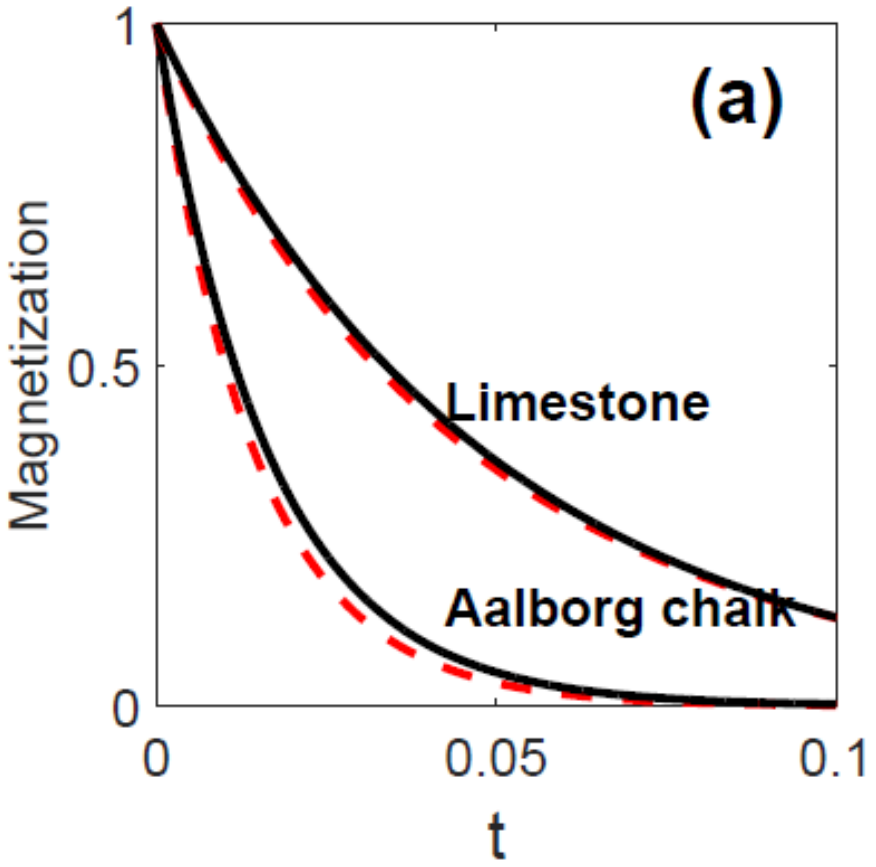


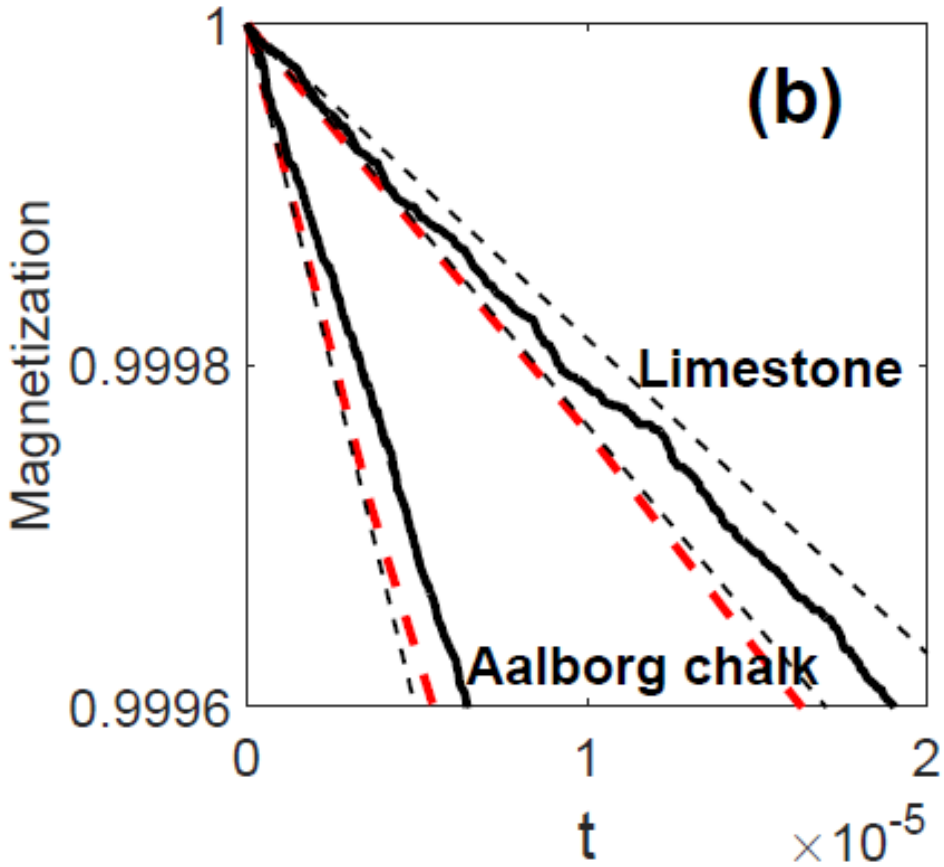

## 5. Discussion and summary

For the NMR relaxation simulation described here, we started from a deterministic partial differential equation and then used an equivalent stochastic particle formulation for the calculation. As expected from the previous investigation [15], the systematic errors for the NMR relaxation caused by the digitalisation of the 2D surfaces within the 3D geometrical objects occurs qualitatively different depending on the object and its orientation in relation to the coordinate system in a digital image. Here we have quantified those systematic errors and showed how they can be reduced for the ball and the cube in 3D and for an artificial 2D porous media for which comparative finite element calculations were tractable.

For two complex digital domains representing different chalk samples, that had similar porosity, but with substantially different specific area, we found qualitatively different relaxation dynamics. Additionally for each of those complex domains the relaxation curve without local boundary conditions were markably lower and we expect to have removed a major part of the errors between the true NMR relaxation and its simulated dynamics.

use a thin plate in the x-y plane. Then the left hand side ($x = 0$) would have electric potential 1 V and the right hand side ($x = 1$) would have electric potential 0 V. The other two sides are isolated. To solve this analytically with Laplace equation we would have to set up the geometry's boundary conditions, more specifically the Dirichlet boundary condition and the Neumann boundary conditions. So we have to solve,

$$\nabla^2 u = \frac{\partial^2 u}{\partial x^2} + \frac{\partial^2 u}{\partial y^2} = 0, u(0, y) = 1, u(1, y) = 0, u_y(x, 0) = 0, u_y(x, 1) = 0,$$

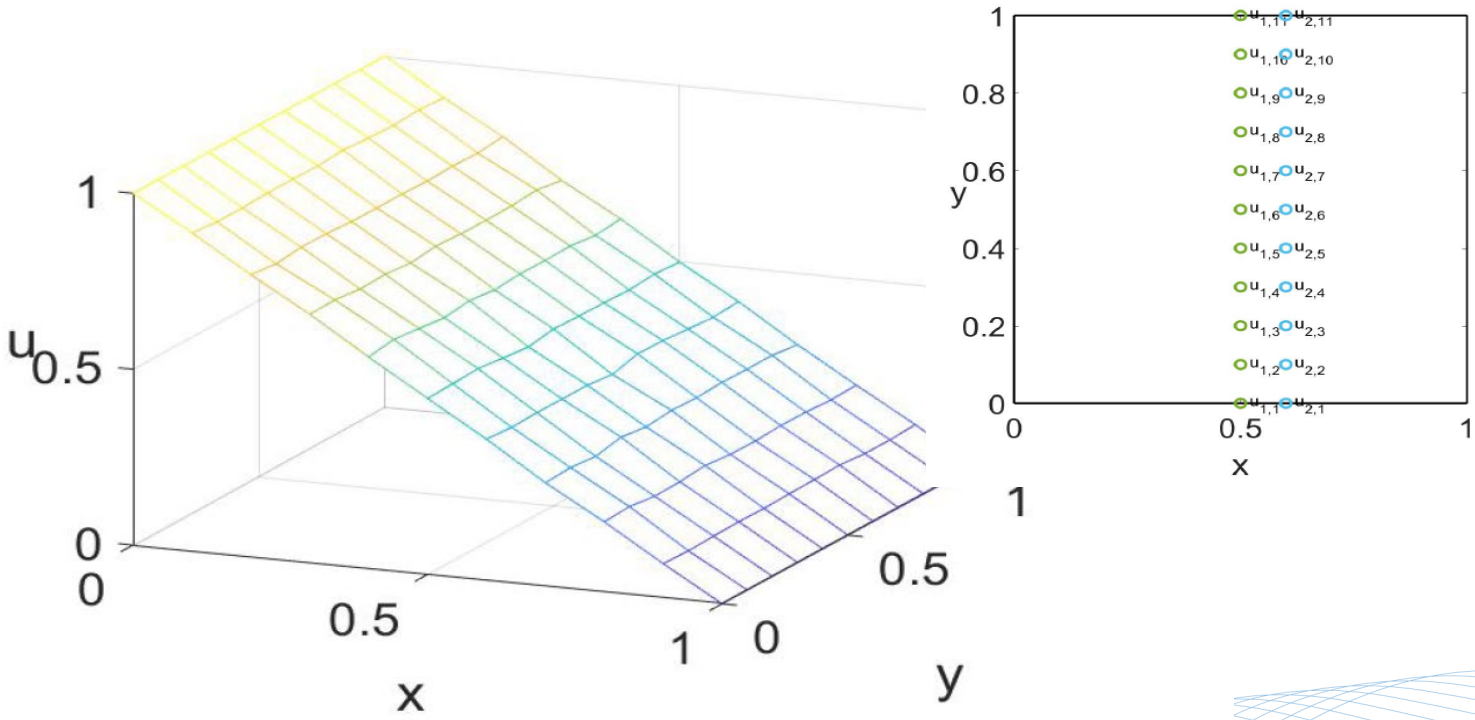


Figure 2.2: The random walk method applied to Eq. (2.2) gives this sloping plane like solution.

# Electric currents….

We compare the random walk solution (RWM) with a solution from Comsol [7]. If we look at the gradient, they are very similar.

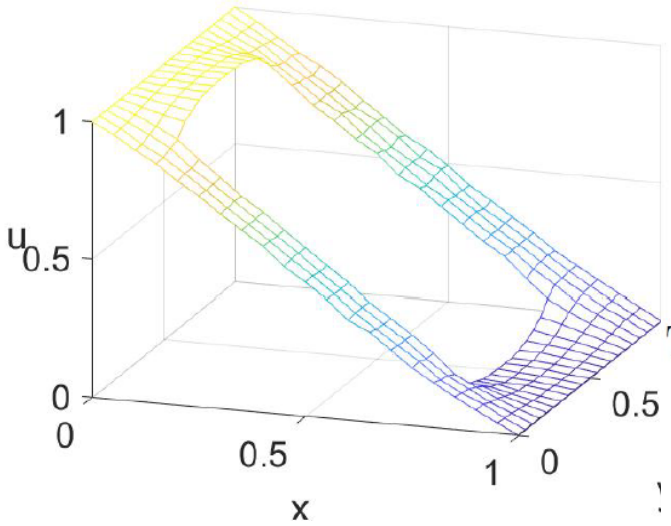


The radius of the central circle is 0.25 m.

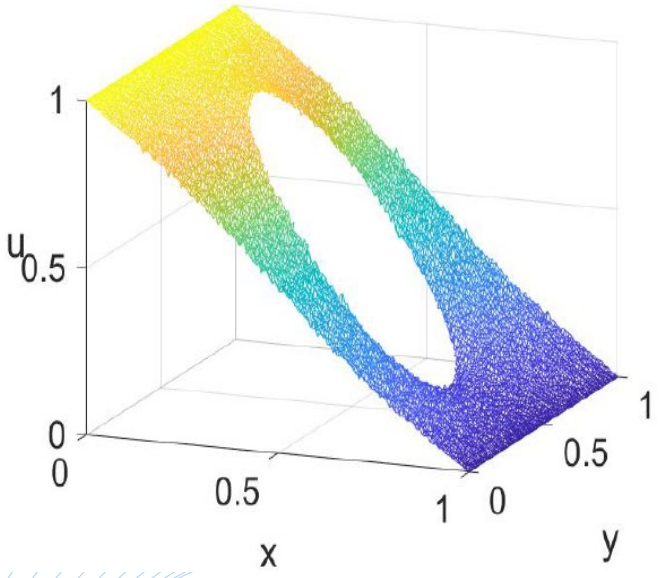

# Electric currents….

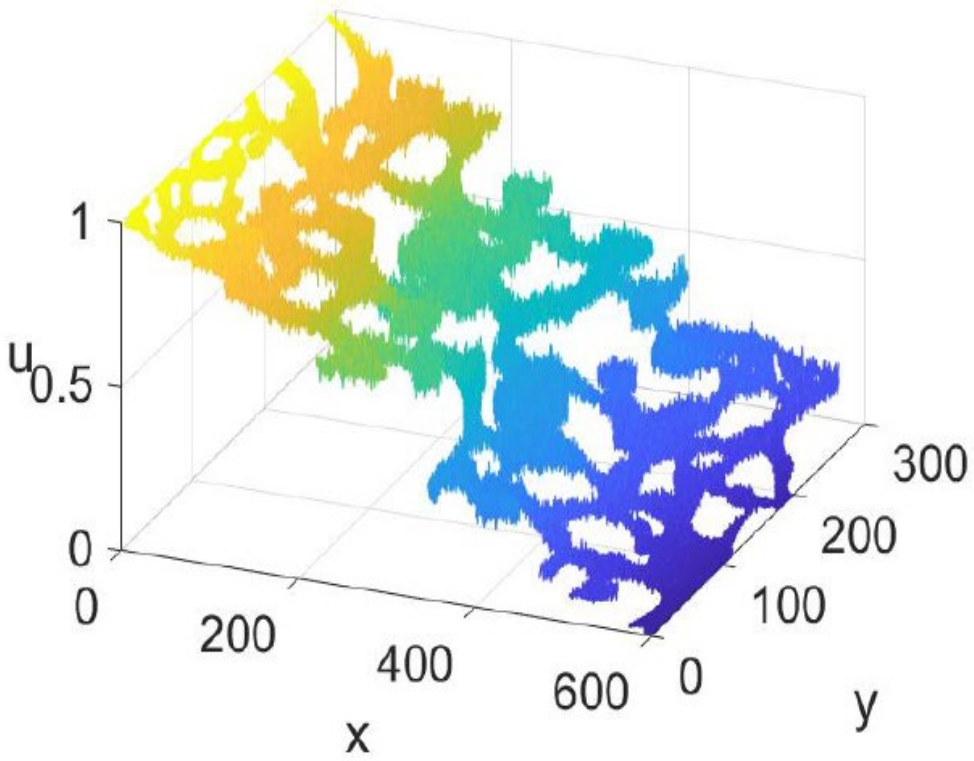


### 3.4.1 Table for the different geometries

| Geometry | Formation factor (RWM) | Formation factor (FEM) |
|---|---|---|
| Square | 2.2339 | 2.2226 |
| Circle | 1.4310 | 1.4885 |
| Porous | 4.2836 | 4.1323 |

# Electric currents….

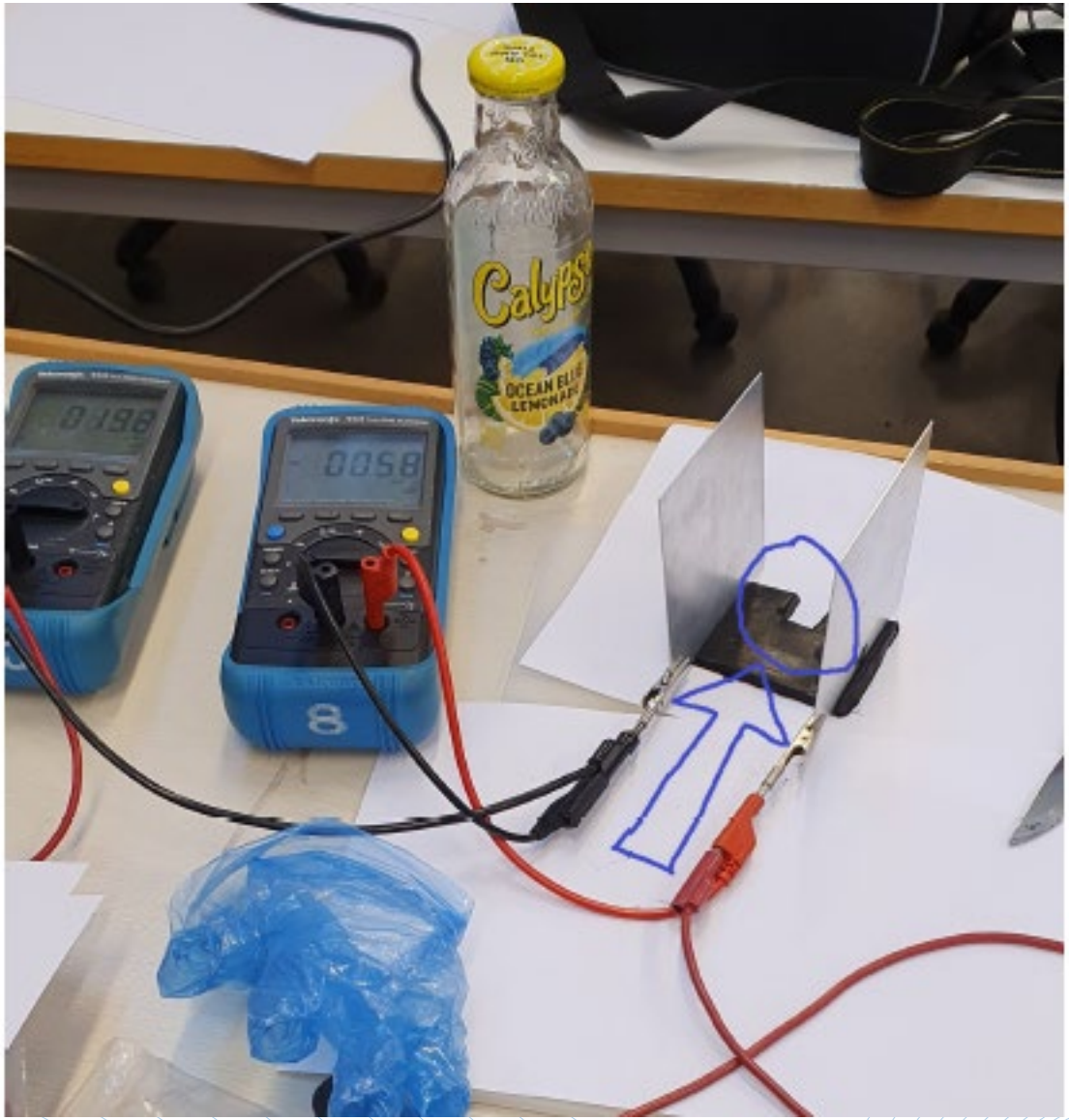

# Electric currents….

and $\sigma = 1$ by comparing with our view

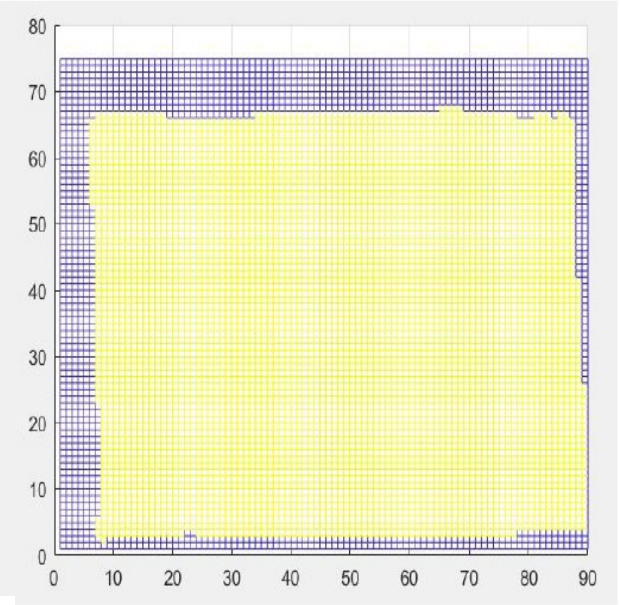


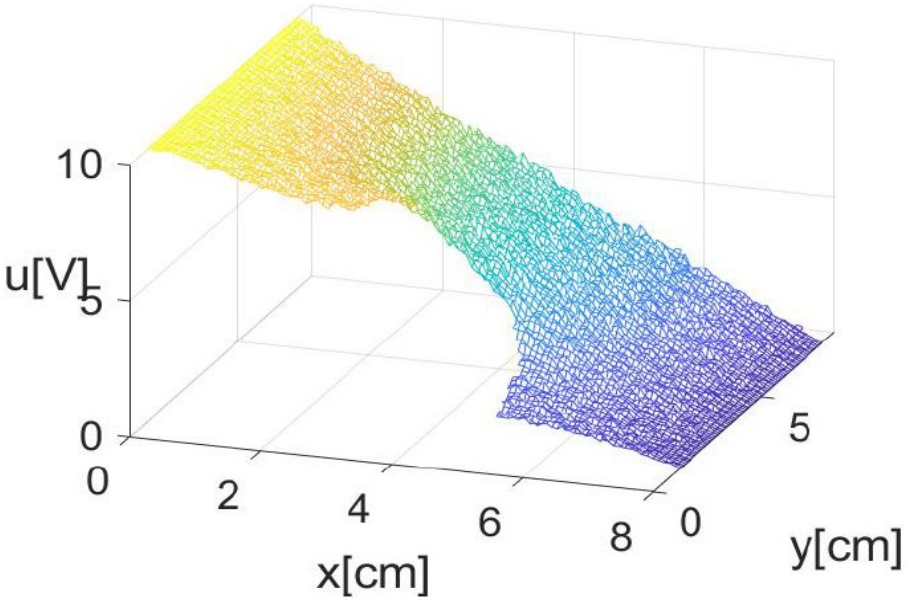


# The Stefan problem

# The heat equation

Consider the problem of determining the temperature profile in a 1D uniform rod of length *L*.

This is solved by the equation

$$\frac{\partial T}{\partial t} = \alpha \frac{\partial^2 T}{\partial x^2}, 0 < x < L$$

Together with appropriate boundary conditions.

# The one-phase Stefan problem

Now consider a 1D rod of ice with an imposed temperature at one end. As the ice melts, water is formed and a moving boundary ***s(t)*** between water and ice is created.

This is the **Stefan Problem.**

# The one-phase Stefan problem

$$\frac{\partial T}{\partial t} = \alpha_L \frac{\partial^2 T}{\partial x^2} \qquad 0 < x < s(t), \qquad t > 0$$

$$T(0,t) = f(t) \qquad t > 0$$

$$T(x,0) = 0$$

$$l\rho \frac{ds}{dt} = -k_L \left.\frac{\partial T}{\partial x}\right|_{x=s(t)} \qquad t > 0$$

$$s(0) = 0 \qquad t > 0$$

$$T\big(s(t)\big) = T_M = 0\ ^\circ\mathrm{C}$$

# The one-phase Stefan problem

In some cases, analytic solutions exist.

With $f(t) = T_0 > 0\ ^\circ C$, the solution is

$$\begin{cases} T(x,t) = T_0\left(1 - \dfrac{\operatorname{erf}(x/(2\sqrt{\alpha_L t}))}{\operatorname{erf}(\lambda)}\right) \\ s(t) = 2\lambda\sqrt{\alpha_L t} \\ \dfrac{c_L}{l}\sqrt{\pi}\lambda e^{\lambda^2}\operatorname{erf}(\lambda) = T_0 \end{cases}$$

# The one-phase Stefan problem

In general, analytic solutions may not exist.

How to model numerically?

Distribute walkers throughout the length, such that $T(x,t) \propto n(x,t)$

Each time step, a walker randomly moves one step left or right.

A walker that reaches the boundary $s(t)$ is absorbed and the boundary moved.

# The one-phase Stefan problem

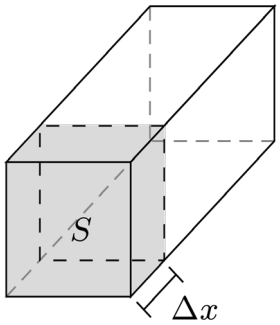


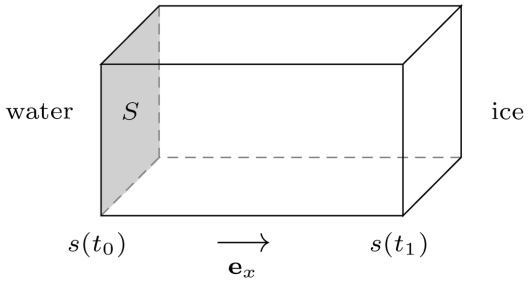


*N* walkers raise the temperature by 1° C.
One walker then carries the heat

$$Q = \frac{S\Delta x \rho c 1°C}{N}$$

Moving the boundary requires the heat

$$Q = S\Delta s \rho l$$

$$\Delta s = \frac{c}{lN}\Delta x$$

Comparison between known analytical solution and RWM solution

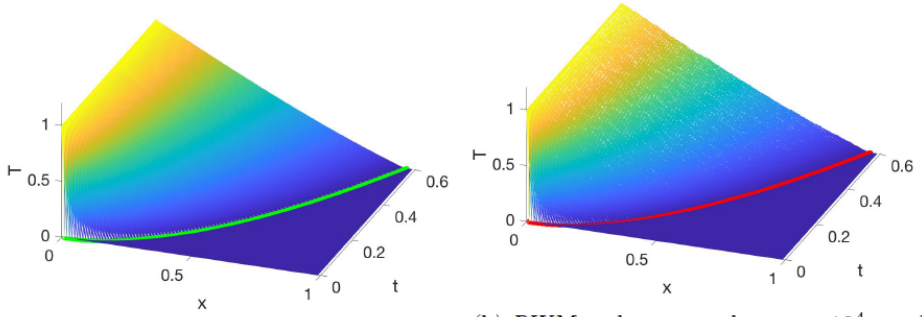


(a) *Analytical solution from (2.8).*

(b) *RWM solution with* $n = 10^4$ *and* $\Delta x = 0.01$.

*Figure 4.3: Solutions for Stefan problem with boundary condition* $f(t) = 1$ *for* $t \in [0, 1]$.

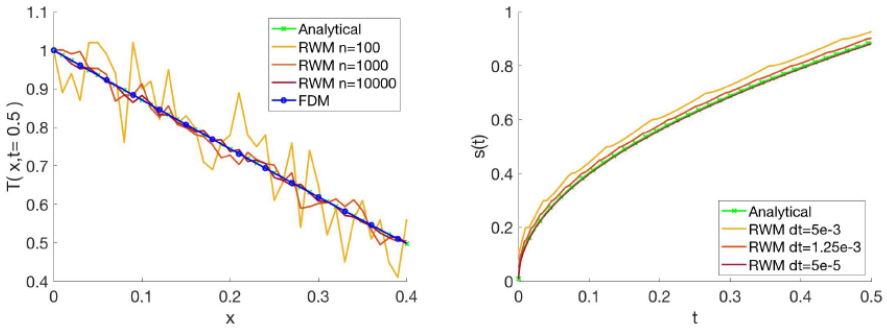


(a) *RWM solutions with* $\Delta x = 0.01$ *and different number of iterations* $n$, *FDM and analytical solutions,* $x \in [0, 0.4]$.

(b) *Solution for the moving boundary* $s(t)$ *with analytical values and RWM for* $n = 10^4$ *and different step lengths* $\Delta t$, $t \in [0, 0.3]$.

*Figure 4.4*

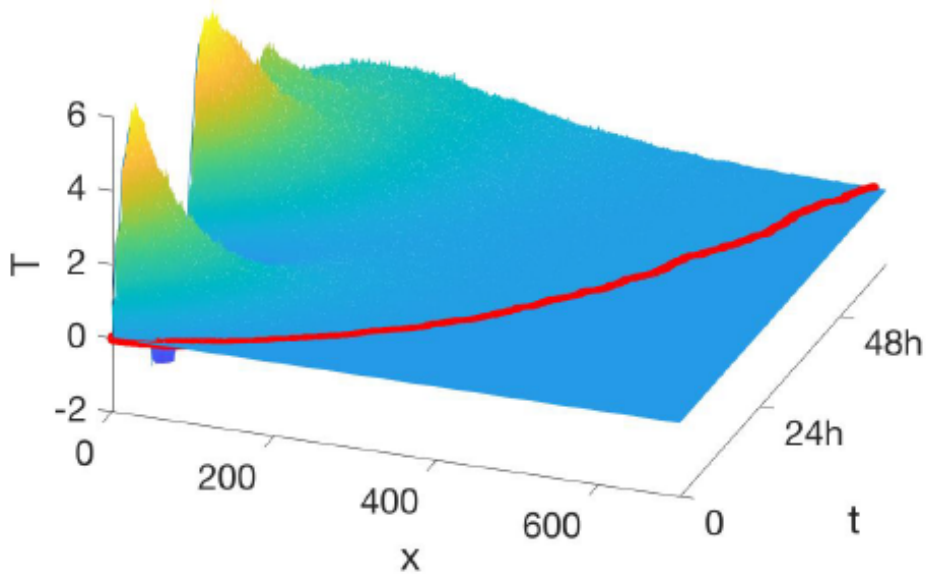


*Figure 4.9: RWM model where $f(t)$ is set to observed day temperatures at Örebro airport 1-3 March 2019. $x$ in mm and $t \in [0, 62\,h]$.*

Results using observed air temperatures as BC.
Note: Negative temperatures in water?

# The two-phase Stefan problem

So far, we've only looked at the water temperature.

No clue as to what's going on in the ice (Assumed T = 0 °C)

No possibility of forming ice if $f(t) < 0$

Need to generalize for two, or more, phases.

# The two-phase Stefan problem

$$\frac{\partial u_L}{\partial t} = \alpha_L \frac{\partial^2 u_L}{\partial x^2} \qquad 0 < x < s(t), \qquad t > 0$$

$$\frac{\partial u_S}{\partial t} = \alpha_S \frac{\partial^2 u_S}{\partial x^2} \qquad s(t) < x, \qquad t > 0$$

$$u_L(0,t) = T_L \qquad t > 0$$

$$u_S(x,0) = T_S(x) \qquad 0 < x$$

$$l\rho \frac{ds}{dt} = -k_L \left.\frac{\partial u_L}{\partial x}\right|_{x=s(t)^-} + k_L \left.\frac{\partial u_S}{\partial x}\right|_{x=s(t)^+} \qquad t > 0$$

$$s(0) = 0 \qquad t > 0$$

$$u_L(s(t)^-, t) = u_S(s(t)^+, t) = T_M = 0\ ^\circ\mathrm{C}$$

# The two-phase Stefan problem

Analytic solutions exist for the two-phase problems as well.

$$\begin{cases} u_L(x,t) = T_L\left(1 - \dfrac{\operatorname{erf}(x/(2\sqrt{\alpha_L t}))}{\operatorname{erf}(\lambda)}\right) \\ u_S(x,t) = T_S\left(1 - \dfrac{\operatorname{erfc}(x/(2\sqrt{\alpha_S t}))}{\operatorname{erfc}(\nu\lambda)}\right) \\ s(t) = 2\lambda\sqrt{\alpha_L t} \end{cases}$$

$$\sqrt{\pi}\lambda = \frac{Ste_L}{\exp(\lambda^2)\operatorname{erf}(\lambda)} + \frac{Ste_S}{\nu\exp(\nu^2\lambda^2)\operatorname{erfc}(\nu\lambda)}, Ste_L = \frac{c_L(T_L - T_M)}{l}, Ste_S = \frac{c_s(T_M - T_S)}{l}, \nu = \sqrt{\alpha_L/\alpha_S}$$

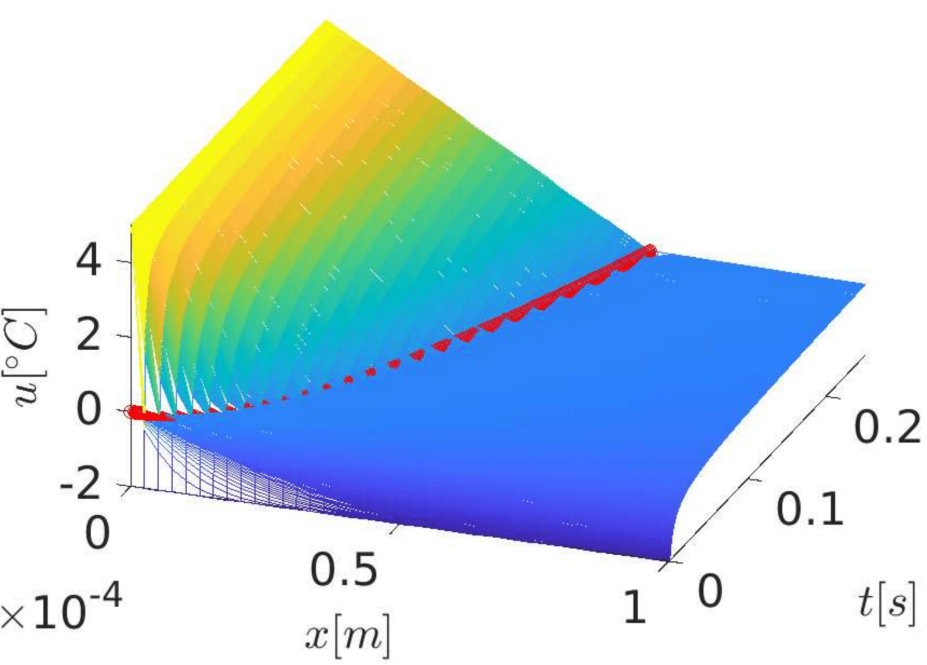
4
2
0
-2
$u[°C]$
0
0.5
1
$\times 10^{-4}$
$x[m]$
0
0.1
0.2
$t[s]$

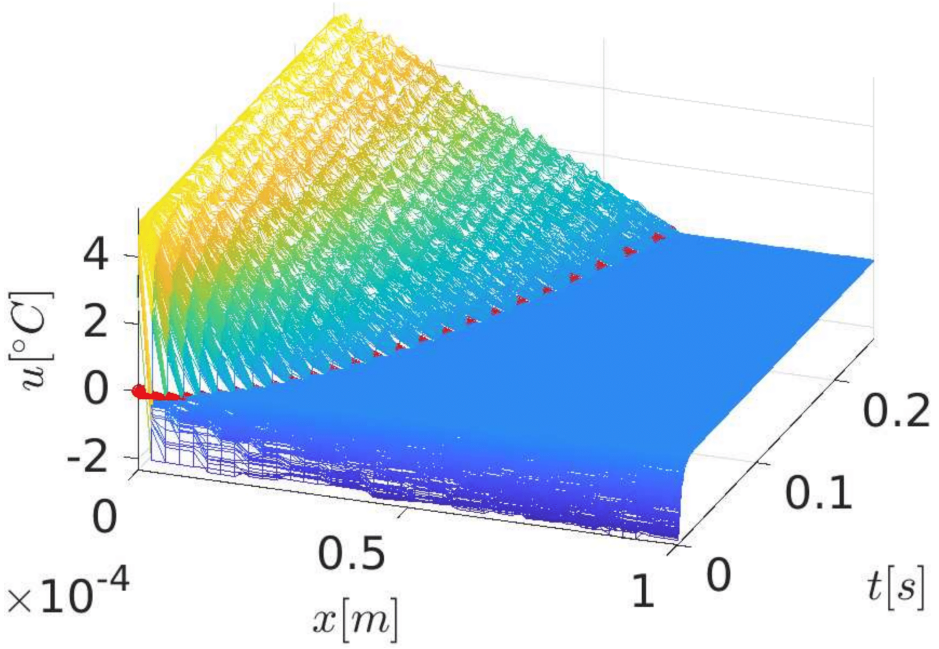
4
2
0
-2
$u[°C]$
0
0.5
1
$\times 10^{-4}$
$x[m]$
0
0.1
0.2
$t[s]$

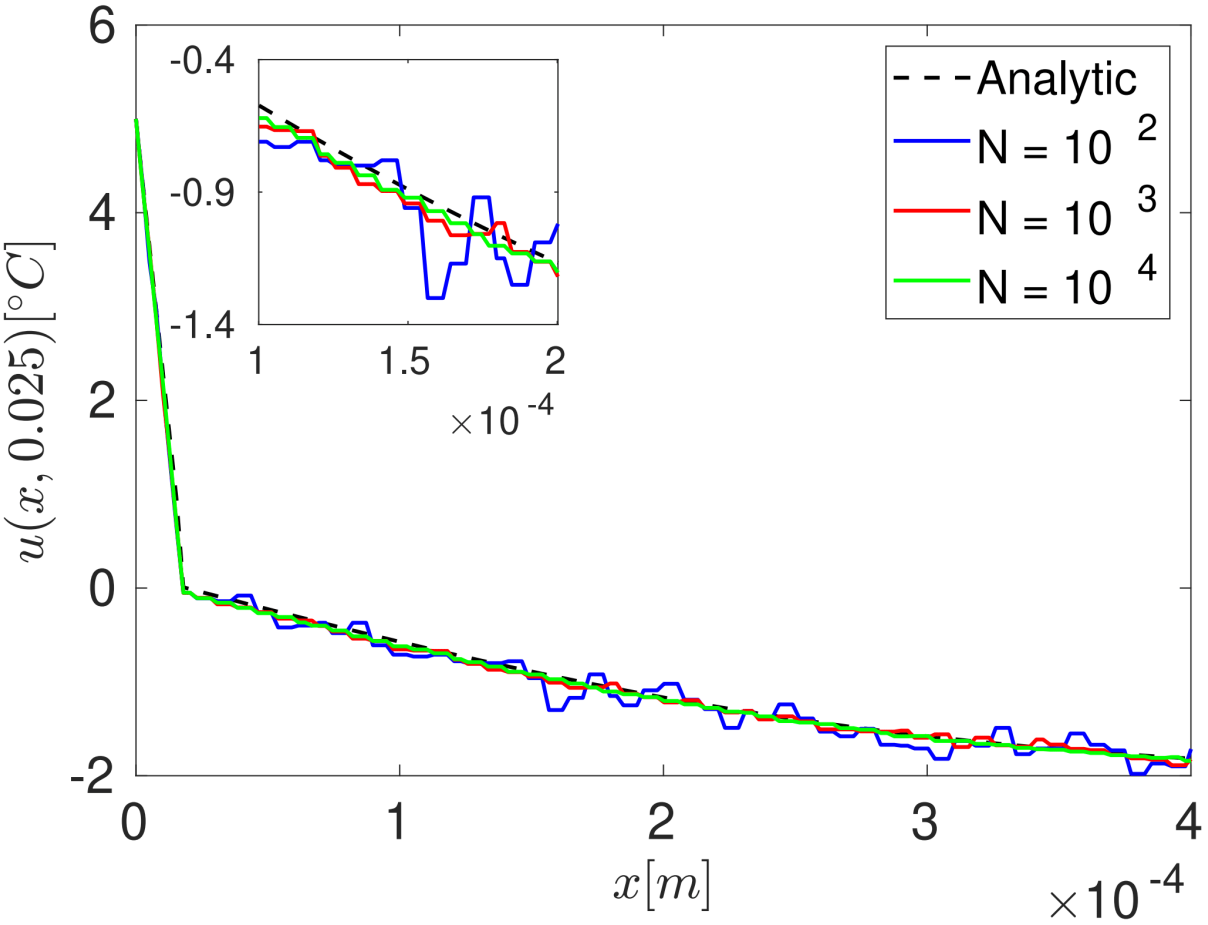
6
4
2
0
-2
0
1
2
3
4
$\times 10^{-4}$
$x[m]$
$u(x, 0.025)[^{\circ}C]$
Analytic
N = 10 2
N = 10 3
N = 10 4
-0.4
-0.9
-1.4
1
1.5
2
$\times 10^{-4}$

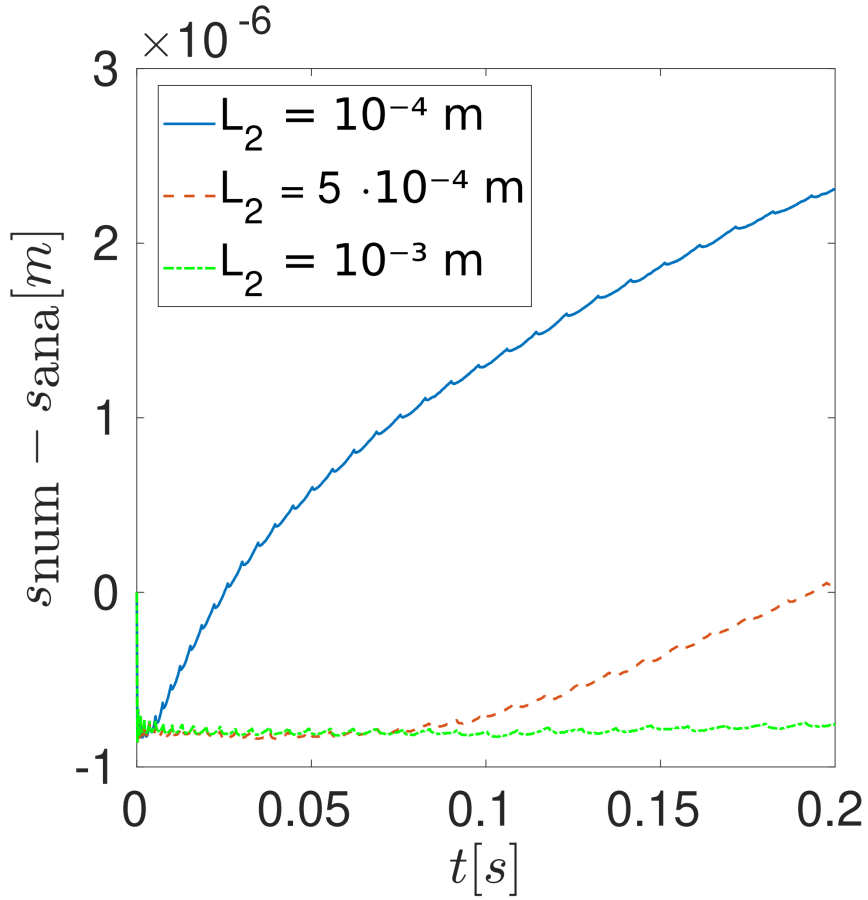
×10 -6
3
2
1
0
-1
$L_2 = 10^{-4}$ m
$L_2 = 5 \cdot 10^{-4}$ m
$L_2 = 10^{-3}$ m
$s_{num} - s_{ana}[m]$
0
0.05
0.1
0.15
0.2
$t[s]$

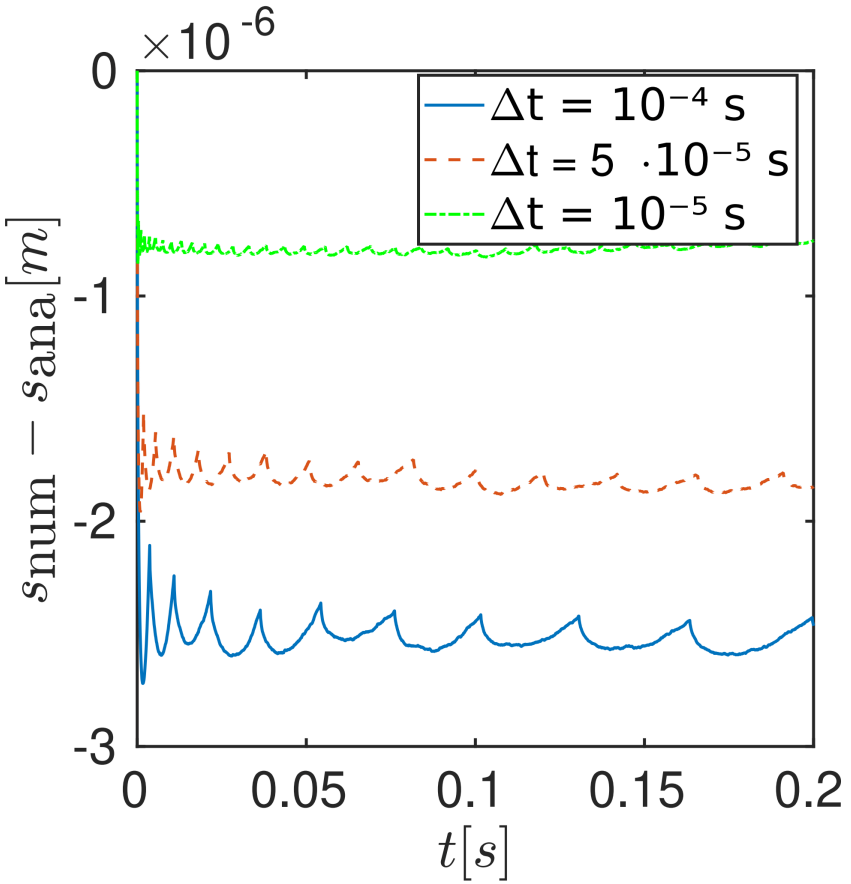
×10 -6
0
-1
-2
-3
$\Delta t = 10^{-4}$ s
$\Delta t = 5 \cdot 10^{-5}$ s
$\Delta t = 10^{-5}$ s
$s_{num} - s_{ana}[m]$
0
0.05
0.1
0.15
0.2
$t[s]$

# Possible extensions

Account for different densities of water and ice.

Consider multiple (variable number of) boundaries

# Non-equal densities, non-constant initial temperature

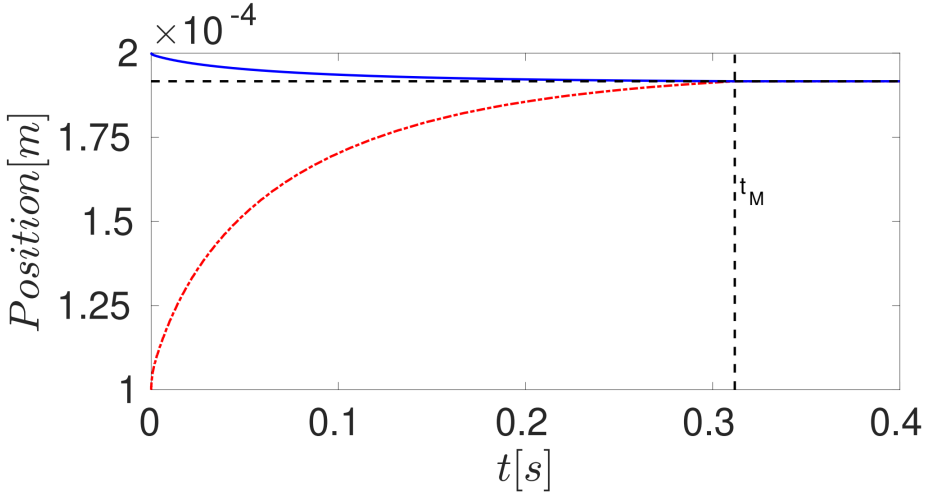


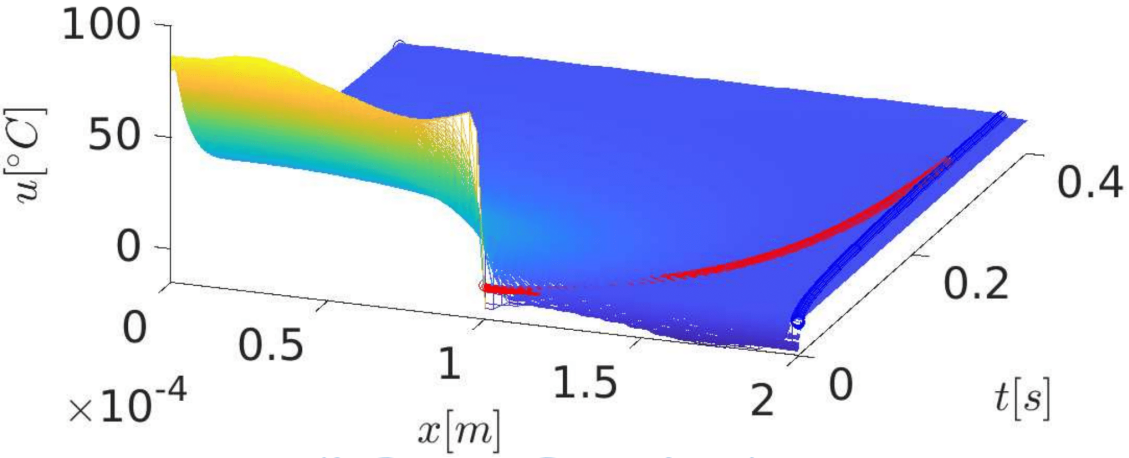

# Three domains

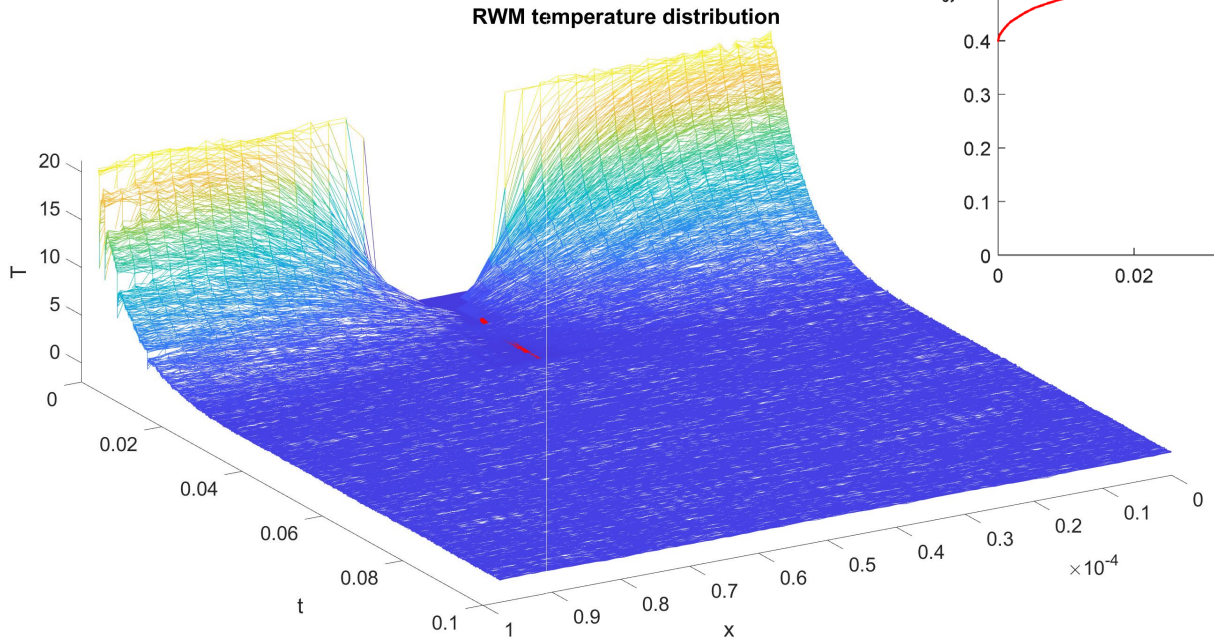


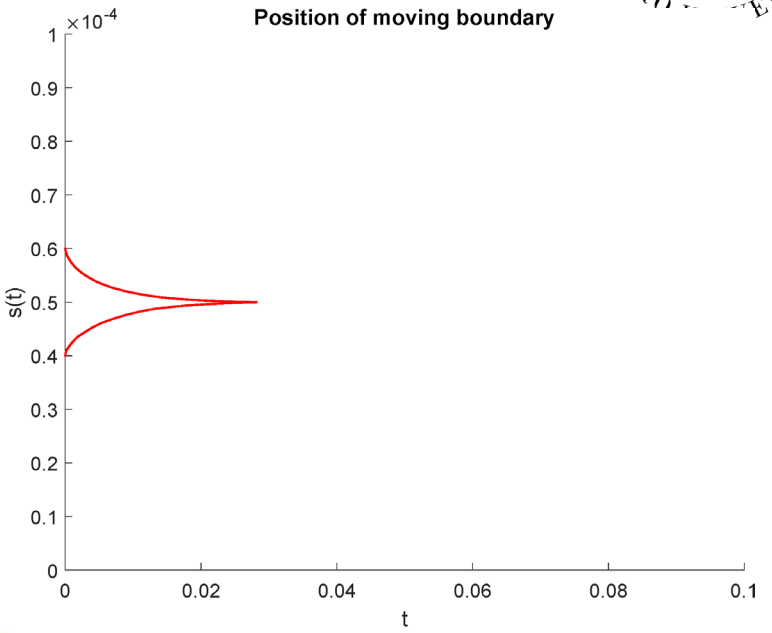


# The Stefan problem

# The role of super-spreaders in modeling of SARS-CoV-2

François Rousse[1], Marcus Carlsson[2], Magnus Ögren[1,3,*], Benjamin Kalischer Wellander[4]

[1]*School of Science and Technology, Örebro University, 70182 Örebro, Sweden*

[2]*Centre for Mathematical Sciences, Lund University, Box 118, 22100 Lund, Sweden*

[3]*Hellenic Mediterranean University, P.O. Box 1939, GR-71004, Heraklion, Greece*

[4]*Centrum för forskning och utveckling (CFUG) Region Gävleborg, Sweden*

**Abstract**

In stochastic modeling of infectious diseases, it has been established that variations in infectivity affect the probability of a major outbreak, but not the shape of the curves during a major outbreak, which is predicted by deterministic models [1]. However, such conclusions are derived under idealized assumptions such as the population size tending to infinity, and the individual degree of infectivity only depending on variations in the infectiousness period. In this paper we show that the same conclusions hold true in a finite population representing a medium size city, where the degree of infectivity is determined by the offspring distribution, which we try to make as realistic as possible for SARS-CoV-2. In particular, we consider distributions with fat tails, to incorporate the existence of super-spreaders. We also provide new theoretical results on convergence of stochastic models which allows to incorporate any offspring distribution with a finite variance.

*Keywords:* COVID-19, compartmental models, SEIR, SIR, offspring distribution for SARS-CoV-2

We use the standard (deterministic) SEIR model

$$\begin{cases} \dot{s}(t) = -\alpha s(t) i(t) \\ \dot{e}(t) = \alpha s(t) i(t) - \sigma e(t) \\ \dot{i}(t) = \sigma e(t) - \gamma i(t) \\ \dot{r}(t) = \gamma i(t) \end{cases} \tag{1}$$

implemented with a step-size of one day (see (8) in Appendix 5.4 for details.) We use the following parameter values; $T_{\text{infective}} = 2.1$, $T_{\text{incubation}} = 4.6$, $\alpha = R_0/T_{\text{infective}}$, $\sigma = 1/T_{\text{incubation}}$ and $\gamma = 1/T_{\text{infective}}$, where $R_0$ is set to 1.3 in all trials.

We first sought to construct a model as close as possible to (1), yet capturing the variability of disease transmission potential between individuals. We model a population of $N$ individuals, each one in a state $z \in \{\mathrm{S}, \mathrm{E}, \mathrm{I}, \mathrm{R}\}$ respectively: susceptible, exposed, infected and recovered. Their state can vary once each day so that we denote by $z_{k,t}$ the state of individual $k$ at day $t$. Each individual has also a personal basic reproduction number $x_k$ drawn once from the offspring distribution. Note that this is the number of people s/he is expected to infect, if s/he becomes infected, assuming that the population is fully susceptible. As immunity builds up, the actual outcome will be less. Hence $x_k$ should be interpreted as the total amount of *potentially infections contacts* (i.e. meetings with other individuals that lead to infection of the other in case s/he is susceptible). Moreover, since $T_{\text{infective}}$ is the average time of infectiousness, this amounts to a rate of $x_k/T_{\text{infectious}} = \gamma x_k$ daily such contacts. We assume that the amount of infectives at any given moment is small compared to the total population, so that each person only meets at most one infective per day, and the total amount of potentially infectious contacts on any given day stays far below the total population, which certainly holds true in our simulations.

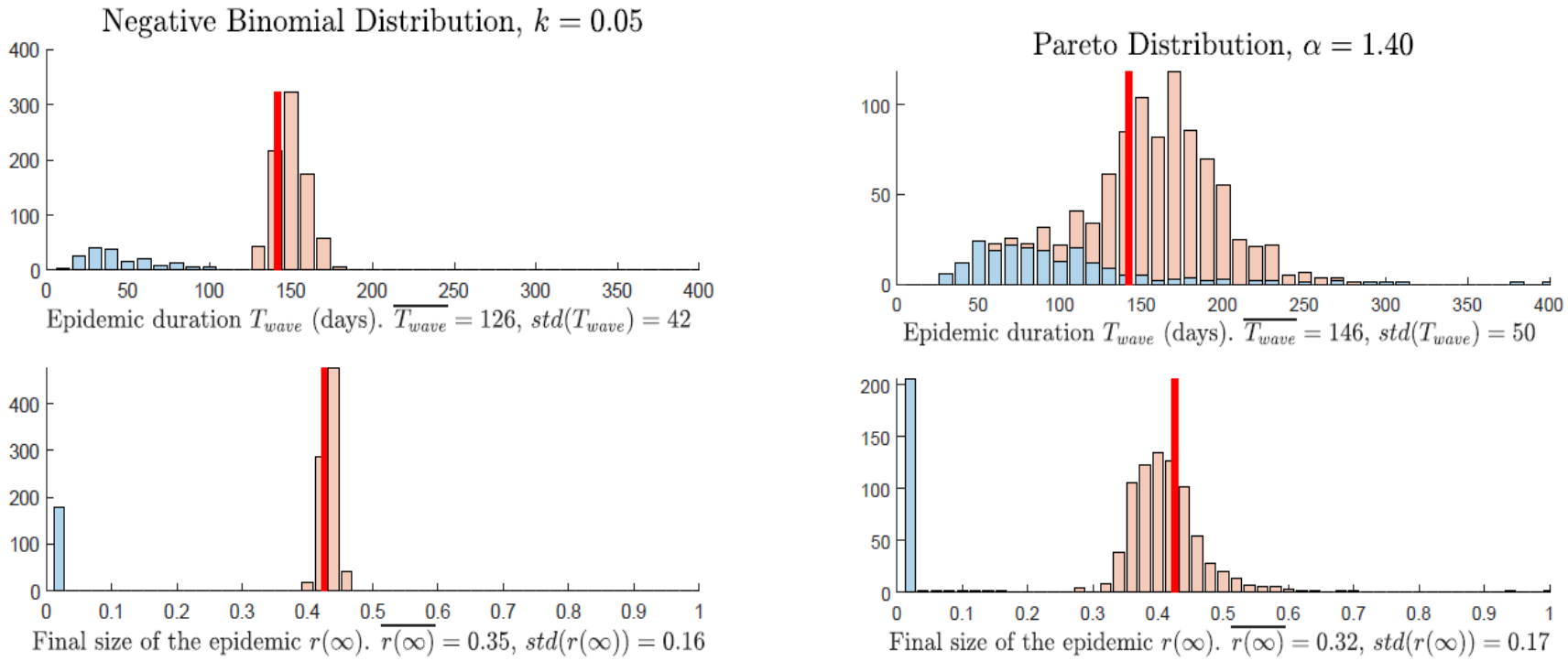


Figure 4: Case (2). A dichotomy appears, either the epidemic becomes self-extinct, or its features are relatively well predicted by the classical SEIR. We differentiate between the two kinds of outcomes by color coding, where blue refers to epidemics going self-extinct and orange refers to epidemics with $r(\infty)$ near the deterministic value $r_\infty$.

# Simulations of quantum dynamics with fermionic phase-space representations using numerical matrix factorizations as stochastic gauges

François Rousse[1], Massimiliano Fasi[1,2], Andrii Dmytryshyn[1], Mårten Gulliksson[1], Magnus Ögren[1,3]
[1] *School of Science and Technology, Örebro University, 70182 Örebro, Sweden*
[2] *Department of Computer Science, Durham University, Stockton Road, DH1 3LE, UK*
[3] *Hellenic Mediterranean University, P.O. Box 1939, GR-71004, Heraklion, Greece*
(Dated: April 12, 2023)

The Gaussian phase-space representation can be used to implement quantum dynamics for fermionic particles numerically. To improve numerical results, we explore the use of dynamical diffusion gauges in such implementations. This is achieved by benchmarking quantum dynamics of few-body systems against independent exact solutions. A diffusion gauge is implemented here as a so-called noise-matrix, which satisfies a matrix equation defined by the corresponding Fokker–Planck equation of the phase-space representation. For the physical systems with fermionic particles considered here, the numerical evaluation of the new diffusion gauges allows us to double the practical simulation time, compared with hitherto known analytic noise-matrices. This development may have far reaching consequences for future quantum dynamical simulations of many-body systems.

A diffusion gauge is manifested by a time-dependent matrix $B \in \mathbb{C}^{n\times m}$ that satisfies the matrix equation

$$D = BB^T, \tag{1}$$

where $D \in \mathbb{C}^{n\times n}$ represents the coefficients of second-order derivatives in the corresponding Fokker–Planck Equation (FPE). By using the operator mappings of the positive-$P$ [3] for bosons and the fermionic Gaussian phase-space representation [1, 2], one can derive the FPE

$$\frac{\partial P(\vec{z})}{\partial t} = -\sum_j \frac{\partial \{a_j(\vec{z})\, P(\vec{z})\}}{\partial z_j} + \frac{1}{2}\sum_{j,k} \frac{\partial^2 \{D_{j,k}(\vec{z})\, P(\vec{z})\}}{\partial z_j \partial z_k}, \quad \vec{z} \in \mathbb{C}^n, \tag{2}$$

for the time-dependent probability distribution $P(\vec{z})$ of bosonic-, fermionic-, or mixed-bosonic-fermionic- systems containing terms with up to four creation- and annihilation-operators in a second quantized Hamiltonian.

We can rewrite the FPE (2) as the Stochastic Differential Equation (SDE) in the Itô interpretation [4]

$$\dot{\vec{z}} = \vec{a}(\vec{z}) + \vec{b}(\vec{z}, \vec{\eta}), \quad \vec{b}(\vec{z}, \vec{\eta}) = B(\vec{z})\, \vec{\eta}, \tag{3}$$

where $\vec{\eta}$ is an $m \times 1$ Gaussian noise vector, and the dot denotes the derivative with respect to time, $d/dt$. We need to construct a matrix $B \in \mathbb{C}^{n\times m}$ that satisfies the matrix equation (1) [4], where $D$ is the matrix in (2). The freedom in $B$ defined by (1) is known as a *diffusion gauge* [5, 6]. This work focuses on the use of diffusion gauges that improves

# Toy model, two bosonic modes [PRA 64, 025801 (2001)]

As an introduction to the use of SDEs for exact quantum dynamics, we begin by revising the well-known time evolution of the one-mode Bose–Hubbard-like Hamiltonian (the Kerr oscillator [15])

$$\widehat{H} = \omega \hat{a}^\dagger \hat{a} + \frac{\chi}{2} \hat{a}^\dagger \hat{a}^\dagger \hat{a} \hat{a}. \tag{4}$$

Note that here and in the remainder of this work we choose our units so that $\hbar = 1$.

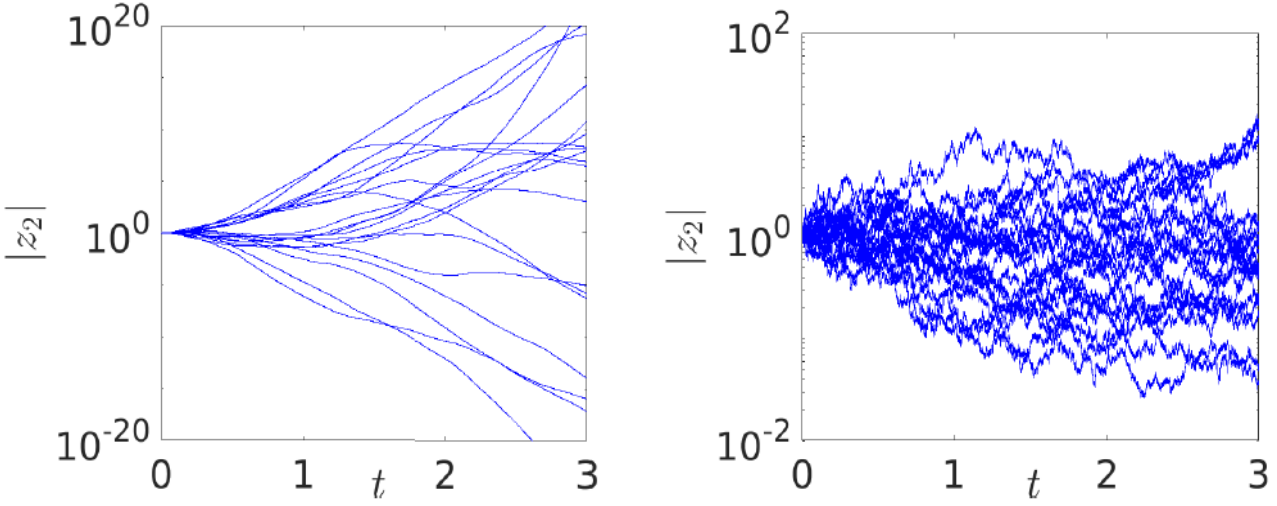


FIG. 1: (Colour online) Positive-$P$ dynamics for 20 individual trajectories with different diffusion gauges. Left: Standard Positive-$P$, with the noise matrix $B$ of equation (A4). Right: "optimal" noise matrix, $B$ of equation (A5) with $\gamma \simeq 3.1985$, see [6]. Note the different scales on the two logarithmic y-axes. Parameters and initial conditions are $\omega = 0$, $N = 10^4$, $\chi = 10^{-2}$ (i.e., $t_{\rm opt} = 1/(\sqrt{N}\chi) = 1$), respectively, according to equation (6), as in [5].

# Toy model, two bosonic modes [PRA 64, 025801 (2001)]

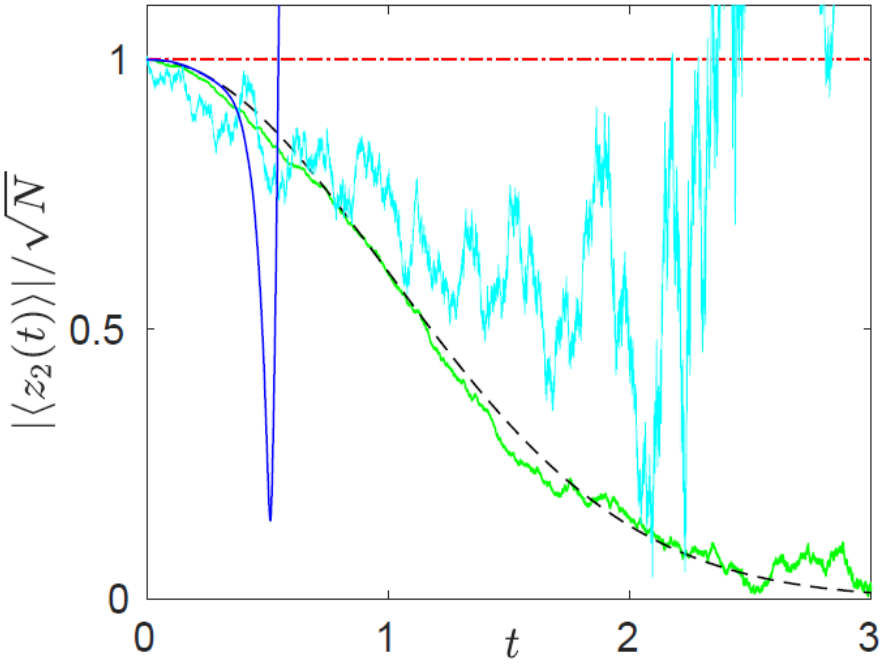


FIG. 2: (Colour online) Benchmarking of the time-dependent correlation function $|\langle\hat{a}^\dagger(t)\hat{a}(0)\rangle|/N = |\langle z_2(t)\rangle|/\sqrt{N}$ as a function of dimensionless time [5]. The dashed (black) curve describe the analytic result of equation (14) in [5]. Solid (blue) curve is numerical results from the phase-space method for $t \leq 0.5$ which is close to the largest useful simulation time with the specific implementation of (5), while the solid (green) curve for $t \leq 3$ shows gauge-improved numerical results using instead a $B$ matrix from equation (A5). We have sampled $10^4$, green solid, and $10^2$, cyan thin, to show the dependence on the number of trajectories. The dashed-dotted (red) horizontal line describe the corresponding Gross-Pitaevskii mean-field result, that do not vary with time in this case. Parameters and initial conditions are the same as in figure 1.

## B. A fermionic Gaussian phase-space representation, for the Fermi–Hubbard model

We study the time evolution of a Fermi–Hubbard Hamiltonian with nearest-neighbour ($\langle i,j\rangle$) jumps and on-site interaction,

$$\widehat{H} = -J\sum\nolimits_{\langle i,j\rangle,\sigma} \hat{c}^{\dagger}_{i,\sigma}\hat{c}_{j,\sigma} + U\sum\nolimits_{j} \hat{n}_{j,\uparrow}\hat{n}_{j,\downarrow}, \tag{7}$$

where $J$ is the hopping amplitude and $U$ the interaction strength. We focus on a small two-site ($j = 1, 2$) chain in order to obtain detailed numerical comparisons for fermionic quantum dynamics.

$$\begin{bmatrix} \dot{z}_1 \\ \dot{z}_2 \\ \dot{z}_3 \\ \dot{z}_4 \\ \dot{z}_5 \\ \dot{z}_6 \\ \dot{z}_7 \\ \dot{z}_8 \end{bmatrix} = i \begin{bmatrix} J\left(z_2 - z_3\right) \\ J\left(z_1 - z_4\right) + U\left(z_5 - z_8\right) z_2 \\ J\left(z_4 - z_1\right) + U\left(z_8 - z_5\right) z_3 \\ J\left(z_3 - z_2\right) \\ J\left(z_6 - z_7\right) \\ J\left(z_5 - z_8\right) + U\left(z_1 - z_4\right) z_6 \\ J\left(z_8 - z_5\right) + U\left(z_4 - z_1\right) z_7 \\ J\left(z_7 - z_6\right) \end{bmatrix} + \sqrt{iU} \begin{bmatrix} i(\tilde{z}_1 z_1 \xi_1 - z_2 z_3 \xi_2) + \tilde{z}_1 z_1 \xi_3 - z_2 z_3 \xi_4 \\ i(\tilde{z}_4 z_2 \xi_2 - z_1 z_2 \xi_1) + \tilde{z}_1 z_2 \xi_3 - z_2 z_4 \xi_4 \\ i(\tilde{z}_1 z_3 \xi_1 - z_3 z_4 \xi_2) + \tilde{z}_4 z_3 \xi_4 - z_1 z_3 \xi_3 \\ i(\tilde{z}_4 z_4 \xi_2 - z_2 z_3 \xi_1) + \tilde{z}_4 z_4 \xi_4 - z_2 z_3 \xi_3 \\ i(\tilde{z}_5 z_5 \xi_1^* - z_6 z_7 \xi_2^*) + \tilde{z}_5 z_5 \xi_3^* - z_6 z_7 \xi_4^* \\ i(\tilde{z}_8 z_6 \xi_2^* - z_5 z_6 \xi_1^*) + \tilde{z}_5 z_6 \xi_3^* - z_6 z_8 \xi_4^* \\ i(\tilde{z}_5 z_7 \xi_1^* - z_7 z_8 \xi_2^*) + \tilde{z}_8 z_7 \xi_4^* - z_5 z_7 \xi_3^* \\ i(\tilde{z}_8 z_8 \xi_2^* - z_6 z_7 \xi_1^*) + \tilde{z}_8 z_8 \xi_4^* - z_6 z_7 \xi_3^* \end{bmatrix}, \tag{8}$$

where the notation $\tilde{z}_j \equiv 1 - z_j$ is used for the so-called hole-variables. In (8), we use the complex noise

$$\xi_j = \frac{\eta_1^{(j)} + i\eta_2^{(j)}}{\sqrt{2}}, \quad j = 1, 2, 3, 4, \tag{9}$$

where $\eta_1^{(j)}$ and $\eta_2^{(j)}$ denote real Gaussian noises with zero mean and unit variance. The complex Gaussian noises $\xi_j$

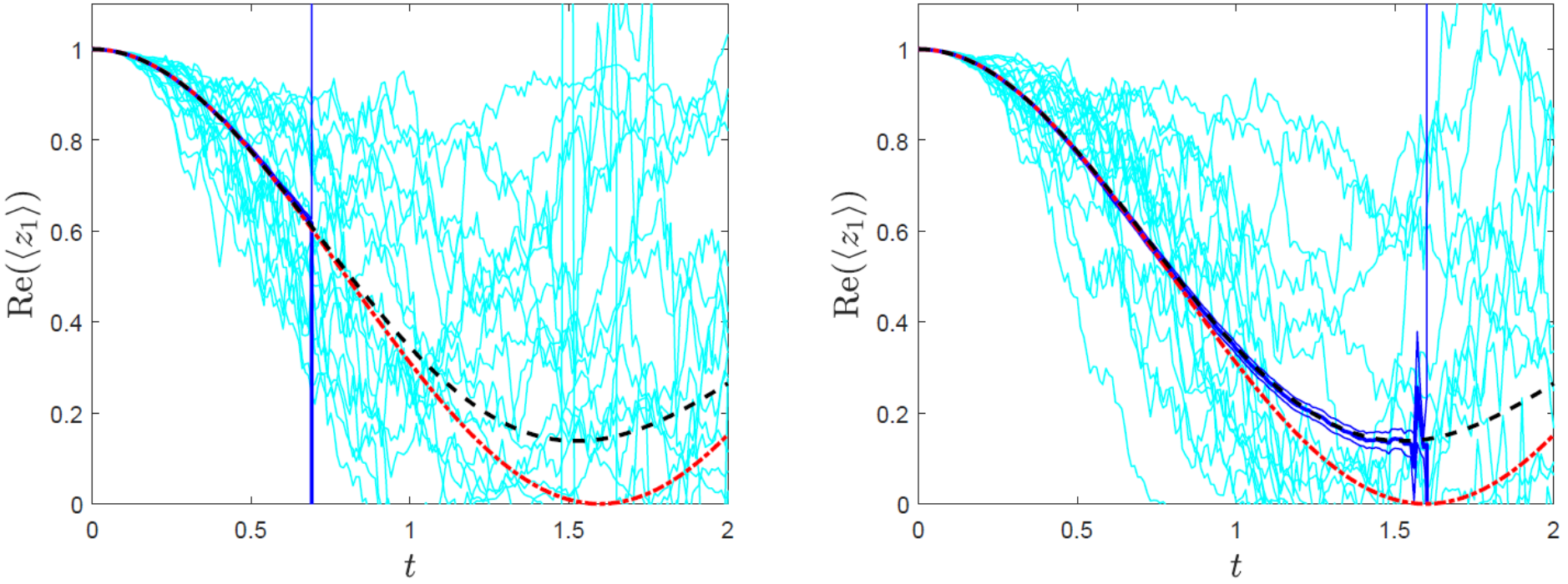


FIG. 3: (Colour online) The occurrence of spikes in the stochastic dynamics for the Fermi–Hubbard model for individual trajectories with different diffusion gauges. Left: Standard GPSR from the literature [14], i.e., with the analytic noise matrix $B$ of equation (A9). Right: GPSR with numerical noise matrices $B$, i.e., dynamically solving equation (1). Thin (cyan) curves are individual trajectories. Thick (blue) curves are the average of $10^3$ such trajectories, surrounded by $\pm$ the stochastic errors. Dashed-dotted (red) curves are from the corresponding Hartree–Fock meanfield-method [19], while dashed (black) curves are from numerical exact diagonalization, for comparisons. Parameters and initial conditions are $J = U = 1$, respectively, according to (12).

### C. A mixed Fermi–Bose phase-space representation, for dissociation of molecules

As an example of a bosonic-fermionic system, we consider the dissociation of a molecular BEC of dimers into pairs of fermionic atoms, with the Hamiltonian

$$\widehat{H} = \hbar \sum\nolimits_{\mathbf{k},\sigma} \Delta_{\mathbf{k}} \hat{c}^{\dagger}_{\mathbf{k},\sigma} \hat{c}_{\mathbf{k},\sigma} - i\hbar\kappa \sum\nolimits_{\mathbf{k}} \left( \hat{a}^{\dagger} \hat{c}_{\mathbf{k},\uparrow} \hat{c}_{-\mathbf{k},\downarrow} - \hat{c}^{\dagger}_{-\mathbf{k},\downarrow} \hat{c}^{\dagger}_{\mathbf{k},\uparrow} \hat{a} \right), \tag{10}$$

where $\Delta_{\mathbf{k}} = \Delta + \hbar\mathbf{k}^2/(2m)$ is a parameter for the kinetic energy of the free atoms, translated with respect to the energy for the bound molecular state [12], and $\kappa$ is the strength of the atom-molecular coupling.

Here, we write down the minimal system with the 5 phase-space variables ($z_1 = n_1$, $z_2 = m_1$, $z_3 = m_1^{+}$, $z_4 = \alpha$, $z_5 = \alpha^{+}$, compare to [12]) in explicit form. From equations (A10) and (A13) in Appendix A, we have the system of SDEs $\dot{\vec{z}} = \vec{a}(\vec{z}) + \vec{b}(\vec{z}, \vec{\eta})$ [12], where

$$\begin{bmatrix} \dot{z}_1 \\ \dot{z}_2 \\ \dot{z}_3 \\ \dot{z}_4 \\ \dot{z}_5 \end{bmatrix} = \begin{bmatrix} \kappa\left(z_3 z_4 + z_2 z_5\right) \\ -2i\Delta_1 z_2 + \kappa z_4\left(1 - 2z_1\right) \\ 2i\Delta_1 z_3 + \kappa z_5\left(1 - 2z_1\right) \\ -\kappa z_2 \\ -\kappa z_3 \end{bmatrix} + \sqrt{\kappa} \begin{bmatrix} z_1\left(z_2\xi_1^{*} + z_3\xi_2^{*}\right) \\ z_2^2\xi_1^{*} - z_1^2\xi_2^{*} \\ -z_1^2\xi_1^{*} + z_3^2\xi_2^{*} \\ \xi_1 \\ \xi_2 \end{bmatrix}. \tag{11}$$

If the noise-terms in (11) are all set to zero ($\xi_j \equiv 0$), then we have a deterministic system that is equivalent to the time-dependent pairing-meanfield formalism [20] for the Hamiltonian (10).

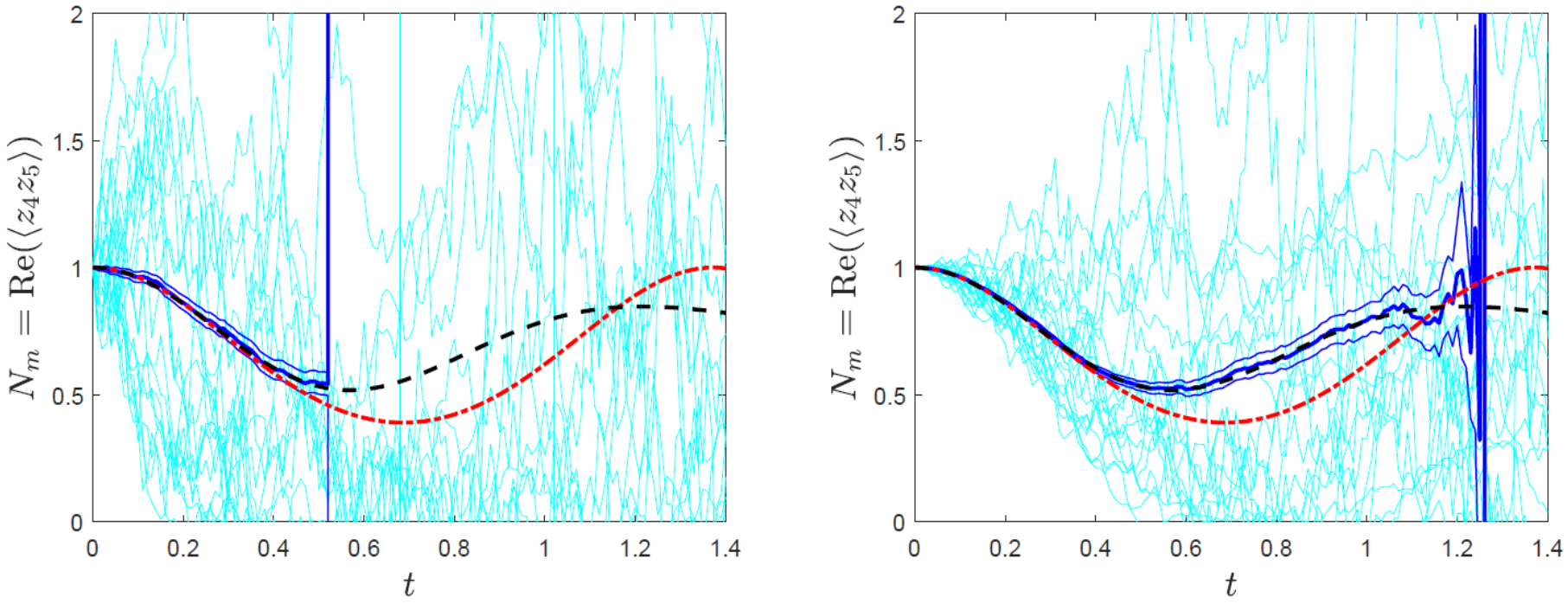


FIG. 5: (Colour online) The occurrence of spikes in the stochastic dynamics for the Fermi–Bose model for individual trajectories with different diffusion gauges. Left: Standard mixed phase-space representation from the literature [12], i.e., with the analytic noise matrix $B$ of equation (A13). Right: GPSR with numerical noise matrices $B$, i.e., dynamically solving equation (1). Thick (blue) curves is the average of $10^3$ such trajectories, surrounded by $\pm$ the stochastic errors. Dashed-dotted (red) curves are from the corresponding pairing-meanfield-method [20], while dashed (black) curves are from numerical exact diagonalization, for comparisons. Parameters and initial conditions are $N_m(0) = \Delta_1 = 1$, and $\kappa = 2$, respectively, according to (16).


# The Stefan problem


# Thank you!

# Questions?